



Available online at [www.sciencedirect.com](http://www.sciencedirect.com)

**ScienceDirect**

Comput. Methods Appl. Mech. Engrg. 401 (2022) 115666

**Computer methods  
in applied  
mechanics and  
engineering**

[www.elsevier.com/locate/cma](http://www.elsevier.com/locate/cma)

# A novel stabilized NS-FEM formulation for anisotropic double porosity media

Qi Zhang<sup>a</sup>, Ze-Yu Wang<sup>a</sup>, Zhen-Yu Yin<sup>a,\*</sup>, Yin-Fu Jin<sup>b</sup>

<sup>a</sup> Department of Civil and Environmental Engineering, The Hong Kong Polytechnic University, Hung Hom, Kowloon, Hong Kong, China

<sup>b</sup> College of Civil and Transportation Engineering, Shenzhen University, Shenzhen, China

Received 10 June 2022; received in revised form 6 September 2022; accepted 18 September 2022

Available online xxxx

## Abstract

Self-consistent extension of linear poroelasticity to overlapping scales of porosity within fluid-saturated anisotropic materials is developed. The coefficient matrix of poromechanical properties considering anisotropy is firstly derived from the corresponding intrinsic properties of its single porosity constituents. The momentum supply term arising from the mass transfer is also quantitatively analyzed. To provide further insight into the theory, numerical values of the poroelastic coefficients are calculated for sandstone that are consistent with the material parameters reported by prominent authors. Then, the node-based smoothed finite element method (NS-FEM) is extended to implement the coupled double porosity flow and deformation formulation. In order to provide numerical stability and accuracy, a modified nodal integration scheme based on multiple stress points over the smoothing domain (SD) and the polynomial pressure projection (PPP) scheme are further implemented in the NS-FEM. Next, four benchmark tests are simulated and compared with reference solutions, based on which the correctness of the proposed NS-FEM formulation is verified and the generalizability of the derived anisotropic double porosity model is confirmed. Finally, the elastoplastic response of double porosity media is investigated, including the impact of permeability anisotropy, the impact of permeability contrast, and the impact of strain-softening.

© 2022 Elsevier B.V. All rights reserved.

**Keywords:** Double porosity; Anisotropy; Finite element method; Nodal integration; Stabilization

## 1. Introduction

In recent years, various theoretical frameworks have been proposed to solve the coupled flow and deformation problems in porous media with double porosity [1–6]. The double porosity is a concept used to describe a certain kind of geologic material [7], which contains connected micro-cracks served as flow channels and nanometer-scale pores in the matrix for fluid storage. In other words, it is used to describe the gradation of pore systems with distinctive storage and transport properties in a continuum framework. This concept was firstly proposed for a non-deformable solid skeleton [8–11], and later it was enriched to consider the effect of solid deformation [12,13]. Most of these coupled frameworks are purely designed for isotropic elastic solid skeleton. Even then, significant disagreement still exists among their theoretical formulations, particularly with the effective stress form and values of pressure coupling coefficients.

\* Corresponding author.

E-mail address: [zhenyu.yin@polyu.edu.hk](mailto:zhenyu.yin@polyu.edu.hk) (Z.-Y. Yin).

Among the formulations, Borja and Koliji [14] and Choo et al. [15] used the mixture theory and continuum principles of thermodynamics to derive an effective stress form, in which various definitions of volume fractions play a central role, resulting from the statistically distributed nature of the pores [16]. This formulation is further generalized in Zhang et al. [17] to incorporate low-velocity non-Darcy flow/transfer and a transversely isotropic permeability tensor due to the preferentially oriented (mainly along the bedding plane) micro-cracks, and is generalized in Zhao and Borja [18] to consider mechanical anisotropy and to recover Biot modulus [19,20], as the Biot modulus is missed in the original Borja and Koliji formulation because of an assumed functional form  $\tilde{f}_s(p^s, \rho^s) = 0$  [14,21]. A modified functional form  $\Gamma(p_s, \phi, p) = 0$  could also reconstruct the Biot modulus [22]. However, a common weakness among these studies is that the evolution law for the binary fraction of porosity ( $\psi^M$  and  $\psi^m$ ,  $\psi^M + \psi^m = 1$ ) cannot be fully specified. As a result, a constant  $\psi^M$  was always adopted in these studies. This weakness was partially resolved in Zhang and Borja [23] by using the principle of superposition and effective stress partition, in which two new superimposed single porosity systems were constructed, namely, the nanopore system and the micro-fracture system. As a result, a new parameter  $C$  was derived, which described the change in internal structure of the material [24]. Besides the mixture theory, the phenomenological approach combined with micromechanics [19] has also been widely used in the deformable double porosity media [3–5,25–27]. While all of them only considered isotropic media, there are very few results for the anisotropic media. Even though an analogous abstract form has been proposed in Zhang [28] and Zhang et al. [29], the specific values used in numerical examples still follow from the mixture theory. The advantage of the phenomenological approach is that the evolution law for  $\psi^M$  or  $\psi^m$  is bypassed, and the aforementioned two new superimposed single porosity systems now have more clear physical meanings, *i.e.*, they are actually two distinct types of porous solid (*porous matrix phase* and *joint phase*) in welded contact with each other, and each of them behaves like a “Gassmann material” [3,26]. The third popular double porosity formulation is proposed by Khalili et al. [2,30–32], in which a new matrix compressibility parameter  $c_p$  was introduced. Compared with the previous two approaches, this approach is less flexible because the theoretical basis for  $c_p$  is missing and only a single  $c_p$  is not enough for anisotropy.

The multiphysics modeling of double porosity media would require sophisticated numerical tools. Among all the numerical tools, the finite element method (FEM) has long been developed to simulate coupled hydromechanical problems [33], while the combined finite element-finite volume approach also becomes more and more popular nowadays for multiphase poromechanics [34–36]. However, the 3-node linear triangular (T3) element tends to give “overly stiff” solution and incurs the volumetric locking due to the violation of Babuška–Brezzi condition [33,37,38]. The poor performance of the T3 element manifests itself in the form of spurious “pressure” oscillation, in which the “pressure” could be the mean stress in incompressible elasticity or the pore pressure in poromechanics [37,39]. To circumvent such problem and employ a broader class of interpolation choices, on one hand, modified variational formulations are proposed to alleviate the incompressibility constraint and increase the stability while maintaining a good convergence behavior [34,37,40–42]. On the other hand, the smoothed finite element method (S-FEM) based on the gradient smoothing technique [43–48] is believed to be able to introduce some advantages from meshfree methods [49] into the FEM interpolation scheme. For instance, S-FEM tends to give “softer” solution that could alleviate the overly stiff problem of FEM with linear triangular element [50–52]. However, despite these efforts, descriptions of the development and application of the stabilized node-based S-FEM into double porosity media is still rare, except in some papers [33,53–55] that describe primary construction for single porosity media.

This paper aims to generalize the framework proposed in Berryman [3] to account for anisotropy and plasticity. In Section 2, we begin by reviewing the results of single porosity theory that are needed in the subsequent analysis. Then new techniques in micromechanics are used to show how the poromechanical constants in the anisotropic theory depend on the physical properties of the microstructural constituents in this complex system. In particular, the poroelastic relations for fluid content variations  $\zeta_1$  and  $\zeta_2$ , and skeleton strain tensor  $e$  under the assumption of infinitesimal deformation are derived. The incorporation of plastic deformation is further discussed for the case of incompressible solid grain and fluid. In Section 3, relevant poroelastic coefficients for Weber sandstone are calculated and compared with those derived by prominent authors. In Section 4, the node-based smoothed finite element method (NS-FEM) is extended to the coupled double porosity flow and deformation problem based on  $\mathbf{u} - p_1 - p_2$  formulation. Additional correction terms are added to the residual in order to circumvent the problem of violation of integration constraints in direct nodal integration and the Babuška–Brezzi condition for equal-order interpolation. The proposed numerical method is then verified by various poroelasticity, reservoir engineering, and biaxial compression benchmark tests in Section 5. Finally, in Section 6, the anisotropic elastoplastic response of double porosity media is investigated.

## 2. Generalized double porosity media

### 2.1. Model assumptions

Before the derivation, it would be beneficial to list the key model assumptions in order to help readers better understand the whole framework and know how one can recover the existing theory. They are given as follows.

- The double porosity media is composed of two distinct single porosity constituents, and each of them is assumed to be anisotropic in the most general situation. The two materials could also differ in stiffness and intrinsic porosity.
- Single porosity theory is applied to the above two single porosity constituents, which are connected to the macroscopic poromechanical coefficients through (i) the strain compatibility relation and (ii) the uniform confining stress condition.
- The formulation given by Zhang and Borja [23] can be derived as a special case of the current formulation when two materials are assigned with the same solid and fluid properties. The significance of  $\mathcal{C}$  in [23] is revealed.
- When two distinct single porosity constituents are isotropic, Berryman's isotropic model [3] is recovered if the effective bulk modulus of the mixture in his derivation is taken as the harmonic average of the constituents' bulk moduli.

### 2.2. Review of single porosity geomechanics

In the absence of external driving forces, the pressures in any types of porosity will be in an equilibrium under the long term limit. Furthermore, as seen in the following sections, extensive use of the single porosity results will be made. It is therefore necessary to remind ourselves of the basic results for single porosity model in anisotropic poroelasticity [56]. The anisotropy is enforced here in order to make the subsequent model development more coherent and consistent. Treating total stress tensor  $\sigma_{ij}$  and fluid (pore) pressure  $p$  as independent variables, the dependent variables are defined to be skeleton strain tensor  $e_{ij}$  and fluid content variation  $\zeta$ , and this choice is termed poroelastic strain–stress relation or pure compliance formulation [57]. According to Cheng [19], this relation is expressed as

$$e_{ij} = S_{ijkl}\sigma_{kl} + \frac{1}{3}DB_{ij}p, \quad (1)$$

$$\zeta = D\left(\frac{1}{3}B_{ij}\sigma_{ij} + p\right), \quad (2)$$

where  $S_{ijkl}$  is the drained elastic compliance tensor, which is the inverse of drained elastic moduli tensor  $C_{ijkl}^e$ , defined by the following relation

$$C_{ijkl}^e S_{klmn} = \frac{1}{2}(\delta_{im}\delta_{jn} + \delta_{in}\delta_{jm}). \quad (3)$$

where  $\delta$  is the Kronecker delta.  $D$  is the constant stress storage coefficient,  $B_{ij}$  is the generalized Skempton pore pressure coefficient tensor. Both  $D$  and  $B_{ij}$  are defined by twenty-one  $C_{ijkl}^e$ , one solid grain bulk modulus  $K'_s$ , and one Biot modulus  $\mathcal{M}$  as [19]

$$D = \frac{1}{\mathcal{M}} + \alpha_{ij}\alpha_{kl}S_{ijkl}, \quad (4)$$

$$B_{ij} = \frac{3S_{ijkl}\alpha_{kl}}{D}, \quad (5)$$

where

$$\alpha_{ij} = \delta_{ij} - \frac{C_{ijkk}^e}{3K'_s} \quad (6)$$

is known as the generalized Biot coefficient tensor.

Before the discussions on double porosity media, it is beneficial to first switch to “engineering notations”. Due to the symmetry of the tensors, all the second order tensors could be expressed as column vectors with 6 components

$$\mathbf{Vec}(\boldsymbol{\sigma}) = [\sigma_{xx} \quad \sigma_{yy} \quad \sigma_{zz} \quad \sigma_{xy} \quad \sigma_{xz} \quad \sigma_{yz}]^T, \quad (7)$$

$$\mathbf{Vec}(\boldsymbol{e}) = [e_{xx} \quad e_{yy} \quad e_{zz} \quad 2e_{xy} \quad 2e_{xz} \quad 2e_{yz}]^T, \quad (8)$$

$$\mathbf{Vec}(\boldsymbol{\alpha}) = [\alpha_{xx} \quad \alpha_{yy} \quad \alpha_{zz} \quad \alpha_{xy} \quad \alpha_{xz} \quad \alpha_{yz}]^T, \quad (9)$$

$$\mathbf{Vec}(\boldsymbol{B}) = [B_{xx} \quad B_{yy} \quad B_{zz} \quad 2B_{xy} \quad 2B_{xz} \quad 2B_{yz}]^T, \quad (10)$$

and fourth-order tensors  $C_{ijkl}^e$  and  $S_{ijkl}$  could be expressed as 6 by 6 square symmetric matrices  $\mathbf{Mat}(\mathbb{C}^e)$  and  $\mathbf{Mat}(\mathbb{S})$ , respectively. Now the constitutive equations Eqs. (1)(2) can be written under the new notation as

$$\begin{bmatrix} \mathbf{Vec}(\boldsymbol{e}) \\ \xi \end{bmatrix} = \begin{bmatrix} \mathbf{Mat}(\mathbb{S}) & \frac{1}{3}D\mathbf{Vec}(\boldsymbol{B}) \\ \frac{1}{3}D\mathbf{Vec}(\boldsymbol{B})^T & D \end{bmatrix} \begin{bmatrix} \mathbf{Vec}(\boldsymbol{\sigma}) \\ p \end{bmatrix}. \quad (11)$$

This now completes the review of the standard results concerning the single porosity compressibility law.

### 2.3. Novel anisotropic double porosity macroscopic constitutive form

In the double porosity formulation, two distinct single porosity constituents are assumed to coexist at the REV level (hereinafter referred to as the material 1 and material 2), whose volume fractions are represented by  $v^{[1]}$  and  $v^{[2]}$ , respectively, with  $v^{[1]} + v^{[2]} = 1$ . Each constituent could have its own porosity ( $\phi^{[1]}$  and  $\phi^{[2]}$ ), which implies the total porosity of the double porosity media is  $v^{[1]}\phi^{[1]} + v^{[2]}\phi^{[2]}$ . A proper double porosity REV should be “large enough compared to the size of the enclosed single porosity constituents so that it may be treated as a homogeneous mixture, and at the same time small enough, compared to the scale of the macroscopic phenomena, so that it may be considered as infinitesimal in mathematical treatment” [58]. Altogether  $\mathbf{Vec}(\boldsymbol{\sigma})$ ,  $p_1$ , and  $p_2$  are treated as independent variables, and the dependent variables are  $\mathbf{Vec}(\boldsymbol{e})$ ,  $\xi_1$ , and  $\xi_2$  [3]. Linear relations among them take the general form, which is also known as the macroscopic compressibility law [3,4]

$$\begin{bmatrix} \mathbf{Vec}(\boldsymbol{e}) \\ \xi_1 \\ \xi_2 \end{bmatrix} = \begin{bmatrix} a_{11} & a_{12} & a_{13} \\ a_{12}^T & a_{22} & a_{23} \\ a_{13}^T & a_{23} & a_{33} \end{bmatrix} \begin{bmatrix} \mathbf{Vec}(\boldsymbol{\sigma}) \\ p_1 \\ p_2 \end{bmatrix}, \quad (12)$$

where the  $a_{11} \in \mathbb{R}^{6 \times 6}$  is a 6 by 6 square symmetric matrix,  $a_{12} \in \mathbb{R}^6$  and  $a_{13} \in \mathbb{R}^6$  are 6 by 1 column vectors, the remaining three parameters  $a_{22}$ ,  $a_{23}$ , and  $a_{33}$  are just scalars. The “anisotropy” is already embedded into this  $3 \times 3$  block matrix.

According to the “Gassmann material” assumption, following two relations also hold that are just analogous to Eq. (11)

$$\begin{bmatrix} \mathbf{Vec}(\boldsymbol{e}^{[1]}) \\ \xi_1/v^{[1]} \end{bmatrix} = \begin{bmatrix} \mathbf{Mat}(\mathbb{S}^{[1]}) & \frac{1}{3}D^{[1]}\mathbf{Vec}(\boldsymbol{B}^{[1]}) \\ \frac{1}{3}D^{[1]}\mathbf{Vec}(\boldsymbol{B}^{[1]})^T & D^{[1]} \end{bmatrix} \begin{bmatrix} \mathbf{Vec}(\boldsymbol{\sigma}^{[1]}) \\ p_1 \end{bmatrix}, \quad (13)$$

$$\begin{bmatrix} \mathbf{Vec}(\boldsymbol{e}^{[2]}) \\ \xi_2/v^{[2]} \end{bmatrix} = \begin{bmatrix} \mathbf{Mat}(\mathbb{S}^{[2]}) & \frac{1}{3}D^{[2]}\mathbf{Vec}(\boldsymbol{B}^{[2]}) \\ \frac{1}{3}D^{[2]}\mathbf{Vec}(\boldsymbol{B}^{[2]})^T & D^{[2]} \end{bmatrix} \begin{bmatrix} \mathbf{Vec}(\boldsymbol{\sigma}^{[2]}) \\ p_2 \end{bmatrix}. \quad (14)$$

Note the volume fractions  $v^{[1]}$  and  $v^{[2]}$  appear here to correct the difference between global fluid content variation and the corresponding local variable for materials 1 and 2.

Now the task is to determine the coupling coefficients between fluid flow and solid deformation shown in Eq. (12) by using the strain compatibility relation  $\boldsymbol{e} = v^{[1]}\boldsymbol{e}^{[1]} + v^{[2]}\boldsymbol{e}^{[2]}$  [26,58] and the condition of uniform stress  $\boldsymbol{\sigma} = \boldsymbol{\sigma}^{[1]} = \boldsymbol{\sigma}^{[2]}$  [25]. After some rearrangements of the terms and expressions, Eqs. (12)(13)(14) are simplified to

$$\begin{aligned} & \left[ a_{11} - v^{[1]}\mathbf{Mat}(\mathbb{S}^{[1]}) - v^{[2]}\mathbf{Mat}(\mathbb{S}^{[2]}) \right] \mathbf{Vec}(\boldsymbol{\sigma}) \\ & + \left[ a_{12} - \frac{v^{[1]}}{3}D^{[1]}\mathbf{Vec}(\boldsymbol{B}^{[1]}) \right] p_1 + \left[ a_{13} - \frac{v^{[2]}}{3}D^{[2]}\mathbf{Vec}(\boldsymbol{B}^{[2]}) \right] p_2 = \mathbf{0}, \end{aligned} \quad (15)$$

$$\left[ a_{12} - \frac{v^{[1]}}{3} D^{[1]} \mathbf{Vec}(\mathbf{B}^{[1]}) \right]^T \mathbf{Vec}(\boldsymbol{\sigma}) + (a_{22} - v^{[1]} D^{[1]}) p_1 + a_{23} p_2 = 0, \quad (16)$$

$$\left[ a_{13} - \frac{v^{[2]}}{3} D^{[2]} \mathbf{Vec}(\mathbf{B}^{[2]}) \right]^T \mathbf{Vec}(\boldsymbol{\sigma}) + a_{23} p_1 + (a_{33} - v^{[2]} D^{[2]}) p_2 = 0, \quad (17)$$

where  $\mathbf{0}$  represents the 6 by 1 zero vector. Since  $\boldsymbol{\sigma}$ ,  $p_1$ , and  $p_2$  are selected arbitrarily [26], their coefficients in above three equations should vanish. Therefore, the  $a_{ij}$  are found as follows

$$a_{11} = v^{[1]} \mathbf{Mat}(\mathbb{S}^{[1]}) + v^{[2]} \mathbf{Mat}(\mathbb{S}^{[2]}), \quad (18)$$

$$a_{12} = \frac{v^{[1]}}{3} D^{[1]} \mathbf{Vec}(\mathbf{B}^{[1]}) = v^{[1]} \mathbf{Mat}(\mathbb{S}^{[1]}) \mathbf{Vec}(\boldsymbol{\alpha}^{[1]}), \quad (19)$$

$$a_{13} = \frac{v^{[2]}}{3} D^{[2]} \mathbf{Vec}(\mathbf{B}^{[2]}) = v^{[2]} \mathbf{Mat}(\mathbb{S}^{[2]}) \mathbf{Vec}(\boldsymbol{\alpha}^{[2]}), \quad (20)$$

$$a_{22} = v^{[1]} D^{[1]}, \quad (21)$$

$$a_{23} = 0, \quad (22)$$

$$a_{33} = v^{[2]} D^{[2]}. \quad (23)$$

From Eq. (18), the inverse of  $a_{11}$  corresponds to the  $\mathbb{C}^e$  of the whole mixture. In Kim et al. [25], this  $\mathbb{C}^e$  is also known as the upscaled elastic tensor at the level of the gridblock from the materials of sub-elements. Usually in the numerical simulation, this  $\mathbb{C}^e$  will be specified directly [17,18,59].

Following some simple linear algebra, Eq. (12) can be modified to the following more familiar form, which is known as the mixed stiffness formulation [57]

$$\boldsymbol{\sigma}'' = \boldsymbol{\sigma} + \boldsymbol{\alpha}_1 p_1 + \boldsymbol{\alpha}_2 p_2, \quad (24)$$

$$\zeta_1 = \boldsymbol{\alpha}_1 : \mathbf{e} + A_{11} p_1 + A_{12} p_2, \quad (25)$$

$$\zeta_2 = \boldsymbol{\alpha}_2 : \mathbf{e} + A_{12} p_1 + A_{22} p_2, \quad (26)$$

where  $\boldsymbol{\sigma}''$  is the effective stress tensor,  $\boldsymbol{\alpha}_1$  and  $\boldsymbol{\alpha}_2$  are Biot tensors,  $A_{ij}$  are components of Biot modulus matrix inverse that are also known as the storage coefficients. All the elements here are functions of  $a_{ij}$  as

$$\mathbf{Vec}(\boldsymbol{\alpha}_1) = a_{11}^{-1} a_{12}, \quad (27)$$

$$\mathbf{Vec}(\boldsymbol{\alpha}_2) = a_{11}^{-1} a_{13}, \quad (28)$$

$$A_{11} = a_{22} - a_{12}^T a_{11}^{-1} a_{12}, \quad (29)$$

$$A_{12} = a_{23} - a_{12}^T a_{11}^{-1} a_{13}, \quad (30)$$

$$A_{22} = a_{33} - a_{13}^T a_{11}^{-1} a_{13}. \quad (31)$$

A fascinating feature of the proposed formulation is that it can be perfectly generalized to the case of multiple porosity. The details are given in [Appendix A](#).

## 2.4. Incorporation of plastic deformation

Above analysis could also be modified to incorporate plastic deformation by adopting the incremental form [60]. Here in order to avoid the debate on the “true effective stress measure” during plastic deformation [18,61],  $K'_s = +\infty$  and  $\mathcal{M} = +\infty$  are assumed to be valid for two single porosity constituents, which makes the Biot effective stress

**Table 1**

Input parameters. The first six parameters are used to construct  $\mathbb{C}^e$  [23] that is positive-definite [66]. BN = bed normal, and BP = bed parallel. Three values of  $\Psi$  are considered, which are  $\Psi = 10, 25, 100$ . In order to apply the formulas in Zhang and Borja [23], the  $a_{11}$  in Eq. (18) will be used.

Parameter	Material 1	Material 2
Young's modulus in BP direction $E_h$ (GPa)	7.8	$7.8/\Psi$
Young's modulus in BN direction $E_v$ (GPa)	5	$5/\Psi$
Poisson's ratio in BP direction $\nu_{hh}$	0.15	0.15
Poisson's ratio in BN direction $\nu_{vh}$	0.2	0.2
Shear modulus in BN direction $G_{vh}$ (GPa)	3	$3/\Psi$
Normal vector to the plane of isotropy $\mathbf{n}$	$\mathbf{e}_z = [0, 0, 1]^T$	$\mathbf{e}_z = [0, 0, 1]^T$
$K'_s$ (GPa)	37.3	37.3
Fluid bulk modulus $K_f$ (GPa)	3.3	3.3
Volume fraction	0.99	0.01
Intrinsic porosity	0.05	0.5

coincide with the Terzaghi effective stress [62]. In addition, these two materials are also assigned with the same material properties. Under this setting, the Biot tensors can be calculated as  $\boldsymbol{\alpha}_1 = v^{[1]} \mathbf{1}$  and  $\boldsymbol{\alpha}_2 = v^{[2]} \mathbf{1}$ , which are consistent with the derived results in Zhao and Borja [18] and Zhang and Borja [23]. For  $A_{11}$ ,  $A_{12}$ , and  $A_{22}$ , they would take the value

$$A_{11}^{-1} = A_{22}^{-1} = -A_{12}^{-1} = \frac{\mathbf{1} : \mathbb{C}^{ep} : \mathbf{1}}{9(v^{[1]}v^{[2]})}, \quad (32)$$

where  $\mathbf{1}$  is the second-order identity tensor and  $\mathbb{C}^{ep}$  is the fourth-order elastoplastic tangential moduli tensor of the whole mixture for any elastoplastic model (the Drucker–Prager model and anisotropic modified Cam–Clay model are specified in this study). As shown in Section 6.1, the variation of  $A_{ij}$  from elastic to elastoplastic deformations is quite small. Therefore, without loss of generality, the  $A_{ij}$  are assumed to be constant even in the plastic deformation range. This assumption will greatly simplify the following numerical formulation and code implementation.

At this moment, the poroelastoplastic relations are fully-determined. These relations should be combined with other governing equations such as the fluid continuity equations to yield a group of useful field equations. These governing equations are provided in previous literature [63–65]. Note the fluid continuity equations are written in a linearized form as the fluid density variation effect has been ignored [19,66]. For the deformation equation, there is an ongoing debate as whether the momentum supply arising as a result of the mass transfer is negligible. This momentum supply is a natural result from Reynolds transport theorem in mixture theory [14,15,17,18,59]. However, it is omitted in many publications [25,28,29,35,67–70] without any strong supporting evidence. In this study, through a scaling analysis and by making use of some published results, a quantitative insight into the influence of this momentum supply term could be obtained. The details are given in Appendix B.

### 3. Comparison of poroelastic coefficients

To further illustrate the use of formulas in Section 2, we compare the calculated values of the poroelastic coefficients with those obtained by other researchers for Weber sandstone [2,4,23] that is well-characterized by laboratory data. To this end, we elucidate the role of stiffness ratio between two materials (porous matrix phase and joint phase) and highlight the transition of Biot coefficients from Zhang and Borja [23] to Berryman and Pride [4].

Table 1 presents a set of input parameters used in these constitutive relations, in which material 2 represents the joint phase and has a higher intrinsic porosity  $\phi^{[2]}$ , a lower volume fraction  $v^{[2]}$ , and a lower stiffness. Here the stiffness of materials is represented by the values of moduli  $E_v$ ,  $E_h$ , and  $G_{vh}$ . Three different stiffness contrasts represented by the value of  $\Psi$  are considered. Tables 2 and 3 display the results of calculations. For a small  $\Psi$ , the proposed approach could match well with that in Zhang and Borja [23] for both Biot tensors and storage coefficients, which suggests the soundness of using pore fractions in mixture theory [23]. For a medium  $\Psi$ , the agreement of the storage coefficients with Berryman and Pride [4] is quite good; and for a high  $\Psi$ , the Biot tensor of material 2 is greater than that of material 1, which provides an explanation to similar findings reported in Berryman and Pride [4] and Khalili and Selvadurai [2]. Furthermore, it is worth mentioning that this approach becomes the second approach that can handle an anisotropic macroscopic system besides Zhang and Borja [23].

**Table 2**

Poroelastic coefficients of the proposed formulation.

Coefficient	$\Psi = 10$	$\Psi = 25$	$\Psi = 100$
Biot tensor component $\alpha_{1x}$	0.8035	0.7063	0.4401
Biot tensor component $\alpha_{1z}$	0.8258	0.7259	0.4523
Biot tensor component $\alpha_{2x}$	0.0907	0.2007	0.5019
Biot tensor component $\alpha_{2z}$	0.0909	0.2009	0.5021
Storage coefficient $A_{11}$ (GPa $^{-1}$ )	0.0562	0.0787	0.1405
Storage coefficient $A_{12}$ (GPa $^{-1}$ )	-0.0208	-0.0459	-0.1149
Storage coefficient $A_{22}$ (GPa $^{-1}$ )	0.0246	0.0527	0.1297

**Table 3**Poroelastic coefficients of Zhang and Borja [23]. The sum of  $\alpha_{1x}$  and  $\alpha_{2x}$  and the sum of  $\alpha_{1z}$  and  $\alpha_{2z}$  are identical to those of Table 2.

Coefficient	$\Psi = 10$	$\Psi = 25$	$\Psi = 100$
Tuned modulus $C$ (GPa)	2.5	1.2	0.5
Biot tensor component $\alpha_{1x}$	0.8121	0.8238	0.8556
Biot tensor component $\alpha_{1z}$	0.8326	0.8417	0.8668
Biot tensor component $\alpha_{2x}$	0.082	0.0832	0.0864
Biot tensor component $\alpha_{2z}$	0.084	0.085	0.0876
Storage coefficient $A_{11}$ (GPa $^{-1}$ )	0.0555	0.0794	0.1437
Storage coefficient $A_{12}$ (GPa $^{-1}$ )	-0.0199	-0.0435	-0.107
Storage coefficient $A_{22}$ (GPa $^{-1}$ )	0.0235	0.0471	0.1107

When  $\Psi = 1$  and two materials have the same intrinsic porosity, the Biot tensors predicted by the proposed formulation will be identical to those in Zhang and Borja [23]. For storage coefficients, they adopt the following values

$$A_{11} = v^{[1]}v^{[2]}D + \frac{v^{[1]}v^{[1]}}{\mathcal{M}} = \frac{\beta v^{[1]}v^{[1]}}{K'_s} + \frac{\phi v^{[1]}}{K_f} + v^{[1]}v^{[2]} \left( C_K^* - \frac{1+\phi}{K'_s} \right), \quad (33)$$

$$A_{22} = v^{[1]}v^{[2]}D + \frac{v^{[2]}v^{[2]}}{\mathcal{M}} = \frac{\beta v^{[2]}v^{[2]}}{K'_s} + \frac{\phi v^{[2]}}{K_f} + v^{[1]}v^{[2]} \left( C_K^* - \frac{1+\phi}{K'_s} \right), \quad (34)$$

$$A_{12} = -v^{[1]}v^{[2]} \left( D - \frac{1}{\mathcal{M}} \right) = \frac{\beta v^{[1]}v^{[2]}}{K'_s} - v^{[1]}v^{[2]} \left( C_K^* - \frac{1+\phi}{K'_s} \right), \quad (35)$$

where  $\beta$  is defined in Eq. (35) of Zhang and Borja [23] and  $C_K^* = S_{iiji}$  (recall  $\mathbb{S}$  is the drained elastic compliance tensor) is defined by Cheng [19]. By comparing above three equations with Eq. (73) of Zhang and Borja [23] and noting that  $\phi^m = \phi v^{[1]}$  and  $\phi^M = \phi v^{[2]}$ , an important relation is obtained

$$\frac{\phi}{C} = v^{[1]}v^{[2]} \left( C_K^* - \frac{1+\phi}{K'_s} \right). \quad (36)$$

Eq. (36) bridges the two formulations in a perfect way since by comparing Eq. (36) with Eq. (66) of Zhang and Borja [23],  $1/K_m^e$  and  $1/K_M^e$  [23] are replaced by the generalized compressibility  $C_K^*$ , and  $K'_s$  is contained in the expression of  $b$  in Zhang and Borja [23]. These excellent correspondences suggest the validity of both formulations.

#### 4. Extension of stabilized NS-FEM formulation

We employ the node-based smoothed finite element formulation in which the main unknown variables are the solid displacement  $\mathbf{u}$  and pore pressures  $p_1$  and  $p_2$  (mixed formulation [17,18]). 2D formulation without gravity is assumed in this study, but an extension to the axisymmetric case [68,71] or 3D should be straightforward. Equal-order (linear T3) interpolation is adopted for the displacement and pressure fields to reduce the computational cost, and a modified nodal integration (NI) is implemented to address the singular mode caused by direct NI [72,73], together with a pressure stabilization term for non-satisfaction of the inf-sup condition when using linear T3 element [33,59]. The key assumptions are listed as follows.

- Only the gradient needs to be smoothed, other terms such as the mass transfer and storage are calculated in the same way as that in the standard FEM procedure.
- Permeability and  $\mathbb{C}^e$  are constant over the whole domain, which greatly simplify the implementation of modified nodal integration and pressure stabilization.
- When solid grain and fluid are incompressible,  $v^{[2]}$  is approaching zero, and the whole system is isotropic, the stabilized NS-FEM formulation would retreat to the formulation proposed by Wang et al. [33] for the basic hydromechanical coupling in geotechnical problems.

In NS-FEM, on top of the element mesh, the problem domain  $\Omega$  is divided into a set of  $N_s$  “non-overlapping” smoothing domains  $\Omega_k^s$  ( $k = 1, 2, \dots, N_s$ ). For NS-FEM, the  $N_s$  is equal to the number of nodes in the standard finite element mesh [43]. The smoothing domain  $\Omega_k^s$  is usually composed of several “non-overlapping” sub-domains  $\Omega_{k,q}^s$  ( $q = 1, 2, \dots, n_k$ ) where  $n_k$  is the number of sub-smoothing domains for  $\Omega_k^s$  [43]. On  $\Omega_k^s$ , the smoothed strain-displacement matrix  $\bar{\mathbb{B}}_k$  is constructed from the compatible strain-displacement matrix  $\tilde{\mathbb{B}}_{k,q}$  on  $\Omega_{k,q}^s$  [33]. Note here  $\tilde{\mathbb{B}}_{k,q}$  is augmented (add some zero columns) from the original  $\mathbb{B}_{3 \times 6}$  matrix for one T3 element to incorporate all the support nodes of  $\Omega_k^s$ . In other words, the size of  $\tilde{\mathbb{B}}_{k,q}$  is  $3 \times 2n_s^k$  where  $n_s^k \geq 3$  is the number of support nodes for  $\Omega_k^s$ . The definition of support nodes of one smoothing domain could be found in Liu and Nguyen [43]. The smoothing operation gives the following expression for  $\bar{\mathbb{B}}_k$  [33,74]

$$\bar{\mathbb{B}}_k = \frac{1}{A_k^s} \sum_{q=1}^{n_k} A_{k,q}^s \tilde{\mathbb{B}}_{k,q}, \quad (37)$$

where  $A_{k,q}^s$  is the area of  $\Omega_{k,q}^s$  and  $A_k^s$  is the area of  $\Omega_k^s$ . The  $A_k^s$  and  $A_{k,q}^s$  satisfy the following equation

$$A_k^s = \sum_{q=1}^{n_k} A_{k,q}^s. \quad (38)$$

From Eq. (37), it is found that  $\bar{\mathbb{B}}_k$  is actually a constant on  $\Omega_k^s$ , and through  $\bar{\mathbb{B}}_k$ , the smoothed strain  $\bar{\mathbf{e}}_k$  on  $\Omega_k^s$  could be calculated. By using the smoothed strain  $\bar{\mathbf{e}}_k$  with constitutive rules, the smoothed stress field  $\bar{\sigma}_k''$  could be calculated. Above operation is exactly the same for the gradient of fluid pressure, and therefore, the “E” matrix used in Zhao and Borja [18] will also be smoothed as

$$\bar{\mathbb{E}}_k = \frac{1}{A_k^s} \sum_{q=1}^{n_k} A_{k,q}^s \tilde{\mathbb{E}}_{k,q}, \quad (39)$$

By using  $\bar{\mathbb{E}}_k$  with Darcy's law, the smoothed Darcy velocities on  $\Omega_k^s$  could be calculated. A simple illustration of the smoothing domain and construction of  $\bar{\mathbb{B}}$  and  $\bar{\mathbb{E}}$  are shown in Fig. 1.

Finally, the FEM matrix equations are provided here. For balance of linear momentum, the residual form is given by

$$\mathcal{R}_u = \mathbf{A} \sum_{k=1}^{N_s} \bar{\mathbb{B}}_k^T \{ \bar{\sigma}_k'' \} A_k^s - \mathcal{K}_{12} \mathbf{p}_1 - \mathcal{K}_{13} \mathbf{p}_2 - \int_{\partial \Omega_t} \mathbb{N}_u^T \hat{\mathbf{t}} \, dA + \varepsilon_s \mathcal{K}_u^{\text{MNI}} (\mathbf{d} - \mathbf{d}^{ln}), \quad (40)$$

$$\mathcal{K}_{12} = \mathbf{A} \sum_{k=1}^{N_s} \left[ \bar{\mathbb{B}}_k^T \int_{\Omega_k^s} \mathbf{Vec}(\boldsymbol{\alpha}_1) \mathbb{N}_{p,k} \, dV \right], \quad (41)$$

$$\mathcal{K}_{13} = \mathbf{A} \sum_{k=1}^{N_s} \left[ \bar{\mathbb{B}}_k^T \int_{\Omega_k^s} \mathbf{Vec}(\boldsymbol{\alpha}_2) \mathbb{N}_{p,k} \, dV \right], \quad (42)$$

$$\mathcal{K}_u^{\text{MNI}} = \mathbf{A} \sum_{k=1}^{N_s} \sum_{q=1}^{n_k} \left( \bar{\mathbb{B}}_k - \tilde{\mathbb{B}}_{k,q} \right)^T \{ \mathbb{C}^e \} \left( \bar{\mathbb{B}}_k - \tilde{\mathbb{B}}_{k,q} \right) A_{k,q}^s, \quad (43)$$

where  $\mathbf{A}$  represents the assembling operator,  $\{ \square \}$  represents the Voigt notation of  $\square$  [60],  $\mathbb{N}_u$  and  $\mathbb{N}_p$  denote the shape functions for displacement and two pressure fields, respectively, and  $\mathbb{N}_{p,k}$  emphasizes the  $\mathbb{N}_p$  on smoothing

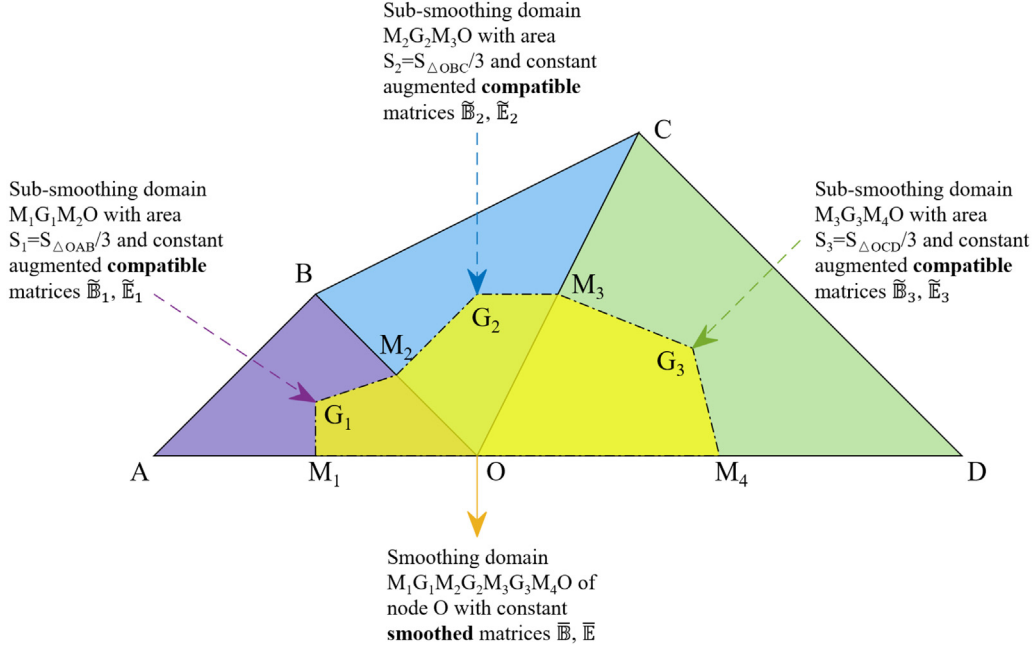


**Fig. 1.** Schematics of the node-based smoothing domain (2D). For the smoothing domain in this figure, the support nodes are {O, A, B, C, D}. The size of the  $\tilde{\mathbb{B}}_i$  matrix is  $3 \times 10$ , and the size of the  $\tilde{\mathbb{E}}_i$  matrix is  $2 \times 5$ .  $\bar{\mathbb{B}}$  is calculated as  $\bar{\mathbb{B}} = (\sum_{i=1}^3 \tilde{\mathbb{B}}_i S_i) / (S_1 + S_2 + S_3)$  and  $\bar{\mathbb{E}}$  is calculated as  $\bar{\mathbb{E}} = (\sum_{i=1}^3 \tilde{\mathbb{E}}_i S_i) / (S_1 + S_2 + S_3)$ .

domain  $\Omega_k^s$ . If  $\alpha_1$  and  $\alpha_2$  are constant over  $\Omega$ , the integration of  $\mathbb{N}_{p;k}$  on  $\Omega_k^s$  could be calculated analytically, see Eq. (39) in Wang et al. [33]. Nodal values of the unknown variables are assembled in the vectors  $\mathbf{d}$ ,  $\mathbf{p}_1$ , and  $\mathbf{p}_2$ .  $\partial\Omega_t$  represents the boundary where surface traction  $\hat{\mathbf{t}}$  is prescribed. The last term on the right-hand side of  $\mathcal{R}_u$  is a modification to the direct nodal integration of NS-FEM where  $\varepsilon_s$  is an integration coefficient. The  $\varepsilon_s$  could be tuned to achieve a balance between the accuracy and numerical oscillation if necessary [49,75–77]. The superscript  $t_n$  represents the converged solution at the previous time step. Note in  $\mathcal{K}_u^{\text{MNI}}$ ,  $\mathbb{C}^e$  is assumed to be constant over  $\Omega$ .

The matrix equations for mass balance are given as

$$\begin{aligned} \mathcal{R}_{p1} = & \left[ \int_{\Omega} A_{11} \mathbb{N}_p^T \mathbb{N}_p dV \right] (\mathbf{p}_1 - \mathbf{p}_1^{t_n}) + \left[ \int_{\Omega} A_{12} \mathbb{N}_p^T \mathbb{N}_p dV \right] (\mathbf{p}_2 - \mathbf{p}_2^{t_n}) + \mathcal{K}_{12}^T (\mathbf{d} - \mathbf{d}^{t_n}) \\ & + \Delta t \mathcal{K}_{22} \mathbf{p}_1 - \Delta t \left[ \int_{\Omega} \gamma \mathbb{N}_p^T \mathbb{N}_p dV \right] (\mathbf{p}_2 - \mathbf{p}_1) - \Delta t \int_{\partial\Omega_{q1}} \mathbb{N}_p^T \hat{\mathbf{q}}_1 dA \\ & + \Delta t \varepsilon_f \mathcal{K}_{p1}^{\text{MNI}} \mathbf{p}_1 + \mathcal{R}_{p1}^{\text{STAB}}, \end{aligned} \quad (44)$$

$$\begin{aligned} \mathcal{R}_{p2} = & \left[ \int_{\Omega} A_{12} \mathbb{N}_p^T \mathbb{N}_p dV \right] (\mathbf{p}_1 - \mathbf{p}_1^{t_n}) + \left[ \int_{\Omega} A_{22} \mathbb{N}_p^T \mathbb{N}_p dV \right] (\mathbf{p}_2 - \mathbf{p}_2^{t_n}) + \mathcal{K}_{13}^T (\mathbf{d} - \mathbf{d}^{t_n}) \\ & + \Delta t \mathcal{K}_{33} \mathbf{p}_2 - \Delta t \left[ \int_{\Omega} \gamma \mathbb{N}_p^T \mathbb{N}_p dV \right] (\mathbf{p}_1 - \mathbf{p}_2) - \Delta t \int_{\partial\Omega_{q2}} \mathbb{N}_p^T \hat{\mathbf{q}}_2 dA \\ & + \Delta t \varepsilon_f \mathcal{K}_{p2}^{\text{MNI}} \mathbf{p}_2 + \mathcal{R}_{p2}^{\text{STAB}}, \end{aligned} \quad (45)$$

$$\mathcal{K}_{22} = \prod_{k=1}^{N_s} \bar{\mathbb{E}}_k^T \frac{\mathbf{k}_1}{\mu_f} \bar{\mathbb{E}}_k A_k^s, \quad (46)$$

$$\mathcal{K}_{33} = \prod_{k=1}^{N_s} \bar{\mathbb{E}}_k^T \frac{\mathbf{k}_2}{\mu_f} \bar{\mathbb{E}}_k A_k^s, \quad (47)$$

$$\mathcal{K}_{p1}^{\text{MNI}} = \prod_{k=1}^{N_s} \sum_{q=1}^{n_k} \left( \bar{\mathbb{E}}_k - \tilde{\mathbb{E}}_{k,q} \right)^T \frac{\mathbf{k}_1}{\mu_f} \left( \bar{\mathbb{E}}_k - \tilde{\mathbb{E}}_{k,q} \right) A_{k,q}^s, \quad (48)$$

$$\mathcal{K}_{p2}^{\text{MNI}} = \prod_{k=1}^{N_s} \sum_{q=1}^{n_k} \left( \bar{\mathbb{E}}_k - \tilde{\mathbb{E}}_{k,q} \right)^T \frac{\mathbf{k}_2}{\mu_f} \left( \bar{\mathbb{E}}_k - \tilde{\mathbb{E}}_{k,q} \right) A_{k,q}^s, \quad (49)$$

$$\begin{aligned} \mathcal{R}_{p1}^{\text{STAB}} &= \left[ \int_{\Omega} \frac{\tau(v^{[1]})^2}{2\bar{G}} [\mathbb{I}_p^T - \Pi(\mathbb{I}_p^T)] [\mathbb{I}_p - \Pi(\mathbb{I}_p)] \, dV \right] (\mathbf{p}_1 - \mathbf{p}_1^{t_n}) \\ &+ \left[ \int_{\Omega} \frac{\tau(v^{[1]}v^{[2]})}{2\bar{G}} [\mathbb{I}_p^T - \Pi(\mathbb{I}_p^T)] [\mathbb{I}_p - \Pi(\mathbb{I}_p)] \, dV \right] (\mathbf{p}_2 - \mathbf{p}_2^{t_n}), \end{aligned} \quad (50)$$

$$\begin{aligned} \mathcal{R}_{p2}^{\text{STAB}} &= \left[ \int_{\Omega} \frac{\tau(v^{[1]}v^{[2]})}{2\bar{G}} [\mathbb{I}_p^T - \Pi(\mathbb{I}_p^T)] [\mathbb{I}_p - \Pi(\mathbb{I}_p)] \, dV \right] (\mathbf{p}_1 - \mathbf{p}_1^{t_n}) \\ &+ \left[ \int_{\Omega} \frac{\tau(v^{[2]})^2}{2\bar{G}} [\mathbb{I}_p^T - \Pi(\mathbb{I}_p^T)] [\mathbb{I}_p - \Pi(\mathbb{I}_p)] \, dV \right] (\mathbf{p}_2 - \mathbf{p}_2^{t_n}), \end{aligned} \quad (51)$$

where  $\gamma$  is the leakage parameter,  $\mathbf{k}_1$  and  $\mathbf{k}_2$  are permeability tensors (constant over  $\Omega$ ), for isotropic tensors,  $\mathbf{k}_1 = k_1 \mathbf{1}$  and  $\mathbf{k}_2 = k_2 \mathbf{1}$  where  $k_1$  and  $k_2$  are scalar permeabilities,  $\mu_f$  is the fluid viscosity (constant over  $\Omega$ ),  $\Delta t$  is the time increment,  $\varepsilon_f$  is also a tunable integration coefficient for modified nodal integration,  $\partial\Omega_{q_1}$  and  $\partial\Omega_{q_2}$  represent boundaries where inward fluxes  $\hat{q}_1$  and  $\hat{q}_2$  are prescribed, respectively. The last two equations Eqs. (50)(51) characterize stabilization terms constructed based on the polynomial pressure projection (PPP) method [33,59,76], in which  $\tau$  is a tunable stabilization parameter,  $\Pi(\square)$  is a projection operator [33], and  $\bar{G}$  is the shear modulus. Sun et al. [78] proposed an automatic estimation technique of the stabilization parameter  $\tau$  for single porosity geomechanics, which considers the compressibility of fluid and solid grains, and the variation of time step and mesh size. In the case of double porosity,  $\tau$  is determined by trial and error. For fluid flow, the advantage of the FEM lies in the treatment of the full-tensor permeability, but if fractional flow happens at the same time, the mimetic finite difference method proposed by Yan et al. [79] is more applicable, especially for anisotropic fractured reservoirs. In this study, the single phase flow is the main focus, thus the use of FEM is justified.

The final step is to solve the system of nonlinear equations using Newton's method. The solution requires construction of an algorithmic tangent operator  $\mathcal{K}$  for use in the linearized equation. Analytical expression for  $\mathcal{K}$  could be easily derived by taking the derivative of  $\mathcal{R}_u$ ,  $\mathcal{R}_{p1}$ , and  $\mathcal{R}_{p2}$  with respect to  $\mathbf{d}$ ,  $\mathbf{p}_1$ , and  $\mathbf{p}_2$  [18].

As a summary to this section, the justifications of the smoothing operation, the use of T3 element, and the computational efficiency are shown in the following bullet form.

- The node-based smoothing domain is automatically generated from a triangular mesh without any human interventions [43]. Only edge midpoints and element centroids are needed in this generation process.
- Although the shape of the smoothing domain (SD) looks irregular in Fig. 1, the smoothed strain-displacement matrix  $\bar{\mathbb{B}}$  is a constant over this SD. Therefore, in the assembly process, the quadrature points of this SD are not needed, as supported by the first term of Eq. (40). All the relevant information is stored in the nodes instead of quadrature points, thus the cost for variable mapping between nodes and quadrature points for FEM is not needed. This is extremely helpful in the large deformation analysis that requires re-meshing strategy [33,53]. For T3 element, the calculation of  $\bar{\mathbb{B}}$  and  $\bar{\mathbb{E}}$  only involves arithmetic weighting average, while for other elements, the calculation requires boundary integration, which is more difficult for code implementation.
- The reason that the T3 element is adopted is because of the evaluation of the modified nodal integration term, as shown in Eq. (43). In a meshfree interpolation scheme, extra evaluation of (smoothed) gradient at

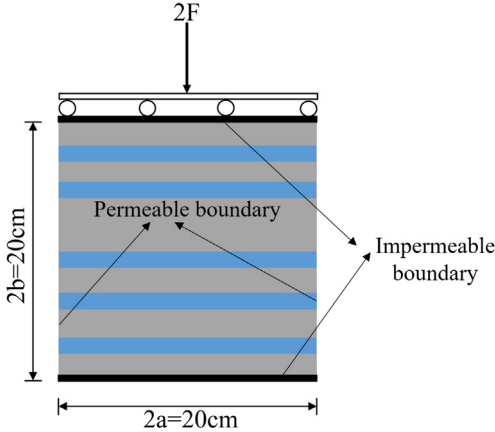


**Fig. 2.** Mandel's problem with transverse isotropy [19,80]. The origin (0, 0) is at the center of the specimen. The mesh size is 2.5 mm.

each additional stress point is unavoidable [76]. However, due to the linear shape function and its piecewise constant derivatives in NS-FEM, these counterparts just take the same value as the compatible gradient matrices  $\tilde{B}$  that have been calculated beforehand, so that no extra computational effort is required, which favors the use of T3 element.

- Compared with the stabilized finite element presented in Choo and Borja [59], the useful PPP technique is also adopted here (but for T3 element), as shown in Eqs. (50)(51). The difference is in the modified nodal integration term that has been calculated in the preprocessing script, and its effect will be illustrated later. In addition, for T3 element, the assembly of the PPP term is very simple since the contribution from each triangle element is purely a constant matrix multiplied by the element area.
- The T3 element is also a good candidate for unstructured mesh (especially with explicit fractures) and local mesh refinement.
- As for the amount of computation, Wang et al. [33] already illustrates the computational efficiency of NS-FEM, compared with the standard FEM. The NS-FEM has the lowest computational time while the results accuracy is still as good as the traditional FEM [33]. Although the formulation in this section does not look as appealing as that in Choo and Borja [59], the actual implementation is easier than it feels like. Furthermore, all the numerical examples used in this manuscript could be computed in a reasonable amount of time.

## 5. Model verification

### 5.1. Transversely isotropic Mandel's problem

Abousleiman et al. [80] derived the analytical solution for transversely isotropic Mandel's problem. This study presents the anisotropic double porosity numerical solution, which should be able to reproduce the previous analytical results. Fig. 2 depicts the geometry of the extended Mandel's problem, which shows a transversely isotropic poroelastic specimen with a cross-section of  $2a \times 2b = 20 \text{ cm} \times 20 \text{ cm}$ , sandwiched between two rigid, frictionless plates. The applied force is  $2F = 2 \times 10^6 \text{ N/m}$ . The datasets for simulation are selected based on the Trafalgar shale provided by Aoki et al. [81]. In order to downgrade from double porosity to single porosity, two ideal cases have been considered [82]. In the first case, it is assumed that the volume fraction of either material 1 or material 2 is reduced to 0. In this study,  $v^{[1]}$  is assumed to be 0, which makes  $\alpha_1 = \mathbf{0}$ . In addition, there would be no mass transfer, which is achieved by setting  $\gamma = 0$ . As a result, the expectation is that the pressure  $p_1$  remains zero for all time, and  $p_2 = p_{\text{ana}}$  where  $p_{\text{ana}}$  is the analytical solution of Abousleiman et al. [80]. In the second case, it has been assumed the properties of material 1 are identical to those of material 2. As a result, the expectation is that  $p_1 = p_2 = p_{\text{ana}}$ , and consequently the numerical solutions would be independent of the value of  $\gamma$ . Table 4 shows the material properties utilized in each case. The simulation runs for 700 uniform time steps with  $\Delta t = 10 \text{ s}$ . Fig. 3 summarizes the main results that are also shown in Abousleiman et al. [80]. Two ideal cases provide consistent numerical results and the agreement with the analytical solutions (Figs. 2, 4, 5, 6 of the

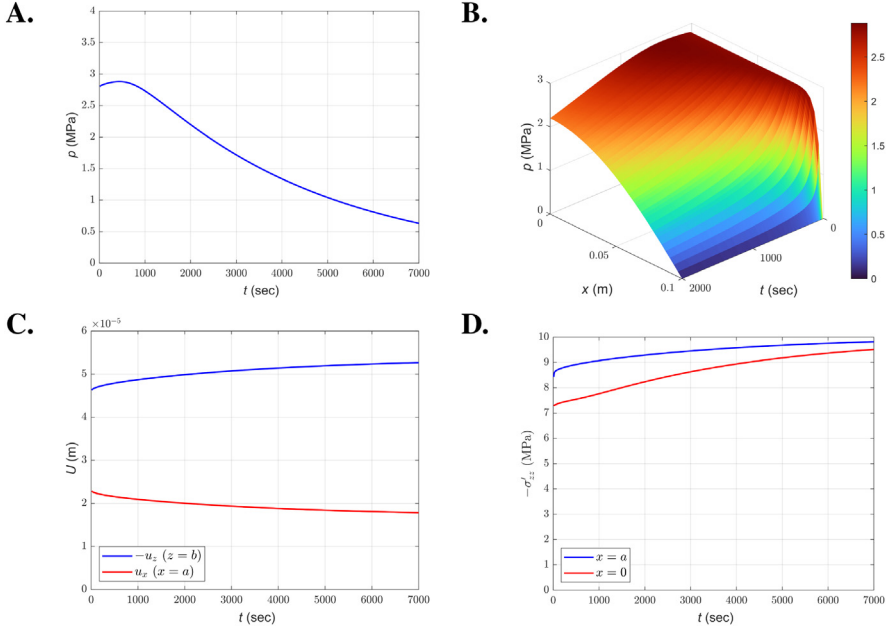


**Fig. 3.** **A.** Pore pressure history at the centerline of specimen ( $x = 0$ ). **B.** Pore pressure history along the  $x$ -axis. **C.** Vertical displacement magnitude at the top (blue line) and horizontal displacement at the right edge (red line). **D.** Terzaghi effective vertical compressive stress  $-\sigma'_{zz}$  history at  $x = 0$  (red line) and  $x = a$  (blue line). Note that  $\sigma'_{zz} = \sigma_{zz} + p$ . (For interpretation of the references to color in this figure legend, the reader is referred to the web version of this article.)

**Table 4**

Material parameters used in the transversely isotropic Mandel's problem [80]. The first six parameters are used to construct  $\mathbb{C}^e$  [23] that is positive-definite [66]. BN = bed normal, and BP = bed parallel. The storage coefficients are multipliers of pressure time derivatives. For modified NI,  $\varepsilon_s = \varepsilon_f = 1$ ; while for PPP,  $\tau = 2$  and  $\bar{G} = G_{vh}$ .

Parameter	Case 1	Case 2
Young's modulus in BP direction $E_h$ (GPa)	20.6	
Young's modulus in BN direction $E_v$ (GPa)	17.3	
Poisson's ratio in BP direction $\nu_{hh}$	0.189	
Poisson's ratio in BN direction $\nu_{vh}$	0.246	
Shear modulus in BN direction $G_{vh}$ (GPa)	7.23	
Normal vector to the plane of isotropy $\mathbf{n}$	$[0, 1]^T$	
Biot modulus $M$ (GPa)	15.8	
Volume fraction $v^{[1]}, v^{[2]}$	0, 1	0.5, 0.5
Biot tensor $\alpha_1$ in vector form	$[0, 0, 0]^T$	$[0.3665, 0.3745, 0]^T$
Biot tensor $\alpha_2$ in vector form	$[0.733, 0.749, 0]^T$	$[0.3665, 0.3745, 0]^T$
Storage coefficient $A_{11}$ (GPa $^{-1}$ )	0	$1/M$
Storage coefficient $A_{22}$ (GPa $^{-1}$ )	$1/M$	$1/M$
Storage coefficient $A_{12}$ (GPa $^{-1}$ )	0	$-1/(2M)$
Permeability tensor $\mathbf{k}_1(x, y)$ (nD)	Arbitrary	50, 10, 0
Permeability tensor $\mathbf{k}_2(x, y)$ (nD)	100, 20, 0	50, 10, 0
Fluid viscosity $\mu_f$ (cP)	1	
Leakage parameter $\gamma$ (Pa $^{-1} \cdot s^{-1}$ )	0	Arbitrary

reference paper) is excellent. It is observed that the pore pressure in the center region rises above the initial value before it dissipates as time progresses. In the horizontal direction, the sample instantaneously expands due to the undrained Poisson's ratio. It then contracts as time goes on and finally approaches the value attributed from the drained Poisson's ratio.

**Table 5**

Material parameters used in the isothermal fractured reservoir problem [83]. Note that  $C^e$ ,  $\varepsilon_s$ , and PPP are not needed in this problem.

Parameter	Value
Volume fraction $v^{[1]}, v^{[2]}$	0.95, 0.05
Aperture of a fracture $\delta$ (m)	$5 \times 10^{-5}$
Shape factor $\sigma_{sh}$ from Warren and Root [9]	60
Fracture spacing $L$ (m)	1
Fracture total compressibility $c_{tf}$ (MPa $^{-1}$ )	0.1
Matrix porosity $\phi_m$	0.05
Matrix total compressibility $c_{tm}$ (MPa $^{-1}$ )	$1.2576 \times 10^{-3}$
Interface permeability $\bar{k}$ (m $^2$ )	$10^{-17}$
$\alpha_1$ and $\alpha_2$ in vector form	[0, 0, 0] $^T$
Storage coefficient $A_{11}$ (MPa $^{-1}$ )	$\phi_m c_{tm}$
Storage coefficient $A_{22}$ (MPa $^{-1}$ )	$3\delta c_{tf}/L$
Storage coefficient $A_{12}$ (MPa $^{-1}$ )	0
Isotropic scalar permeability $k_1$ (m $^2$ )	0
Isotropic scalar permeability $k_2$ (m $^2$ )	$\delta^3/(6L)$
Fluid viscosity $\mu_f$ (Pa · s)	$1.123 \times 10^{-4}$
Leakage parameter $\gamma$ (Pa $^{-1}$ · s $^{-1}$ )	$\sigma_{sh}\bar{k}/(\mu_f L^2)$
Modified NI parameter $\varepsilon_f$	1
Initial reservoir pressure $p_i$ (MPa)	6.078
Reservoir thickness $H$ (m)	1
Wellbore volumetric flow rate $Q_w$ (m $^3$ /s)	$3.125 \times 10^{-5}$
Prescribed inward flux $\hat{q}_2$ (m/s)	$Q_w/(2\pi r_w H)$

## 5.2. Isothermal fluid injection into a double porosity system

We next verify the proposed numerical scheme using an isothermal fractured reservoir problem, for which the reference solution is available from the work of Pruess and Narasimhan [83]. Trial calculations show that fine spatial resolution around the well is required for a satisfactory result. In this study, the same mesh is adopted as that in Pruess and Narasimhan [83], which is depicted in Fig. 4. Parameters for this problem are given in Table 5. The deformation field is deactivated by setting  $\alpha_1 = \alpha_2 = \mathbf{0}$ . It is an isothermal single phase injection problem, with simulation time step chosen to be logarithmically equally spaced between  $10^{-3}$  s to  $10^4$  s (701 steps) and numerical result plotted in Fig. 5. The agreement for pressure  $p_2$  transients is very good, and the numerical result also depicts the change of  $p_1$  at the wellbore. Three distinct stages can be observed from Fig. 5, namely the stage of linear flow in the fissure continuum, stage of transition flow from the fissure continuum to the matrix continuum, and stage of overall flow of the whole system, which is a typical characteristic for naturally fractured reservoir [84]. The red line is also widely used in the well testing analysis [85] to deduce the storage parameter  $\omega$  and interporosity flow parameter  $\lambda$ .

## 5.3. 1D consolidation of a double porosity medium

The third verification example concerns the 1D consolidation of a double porosity column [20]. A porous rectangular medium of 2 m height and 0.2 m width is taken, with the normal displacement of left, right, and bottom edges fixed, as shown in Fig. 6. Only the top surface is permeable. This example has been investigated in Zhang et al. [29] by using Laplace transform and numerical Laplace inversion methods [19,86]. Two different cases are considered in this problem, with parameters given in Table 6. The two cases correspond to the slightly compressible fluid constituent (Case 1) and highly compressible fluid constituent (Case 2). A uniform load of 1 MPa is applied on the drainage surface instantaneously at the first time step. Both cases give a perfect match with the semi-analytical solutions, as indicated in Fig. 7. Fig. 7 also indicates that the fluid compressibility could greatly influence the undrained pressure response through the coefficients  $A_{11}$  and  $A_{22}$ . In Zhang et al. [29], the authors did not show the spatial variation of pressure, while this is easily achieved here. The results are shown in Fig. 8. For slightly compressible fluid, the  $p_1$  would exhibit the “double-shell” characteristic [18,20], while for highly compressible fluid, Mandel–Cryer effect is significant on  $p_1$ . Note in the undrained limit,  $p_1$  is not necessarily equal to  $p_2$  depending on the values of storage coefficients [18].

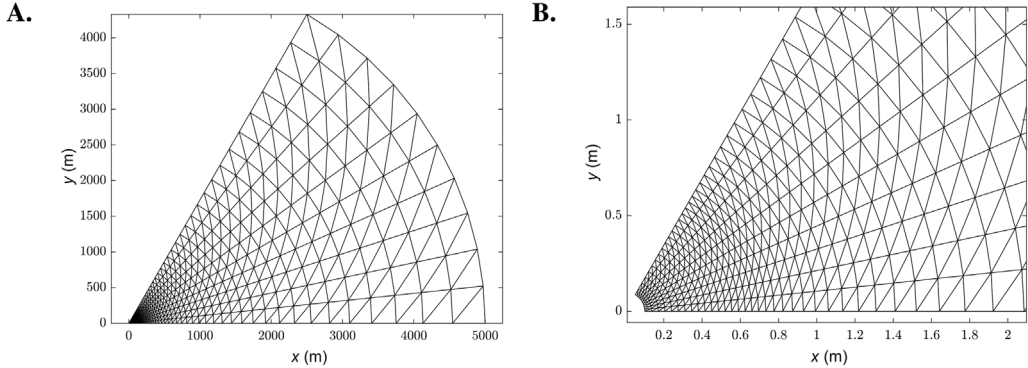


**Fig. 4.** **A.** Mesh of the fractured reservoir. The reservoir external radius  $r_e = 5000$  m, and wellbore radius  $r_w = 0.1$  m. The Dirichlet boundary condition  $p_1 = p_2 = p_i$  is prescribed on the outer boundary  $r = r_e$ , and the Neumann boundary condition (non-zero flux  $\hat{q}_2$ ) for  $p_2$  is prescribed on the inner boundary  $r = r_w$ . **B.** Fine (enlarged) mesh around the well.

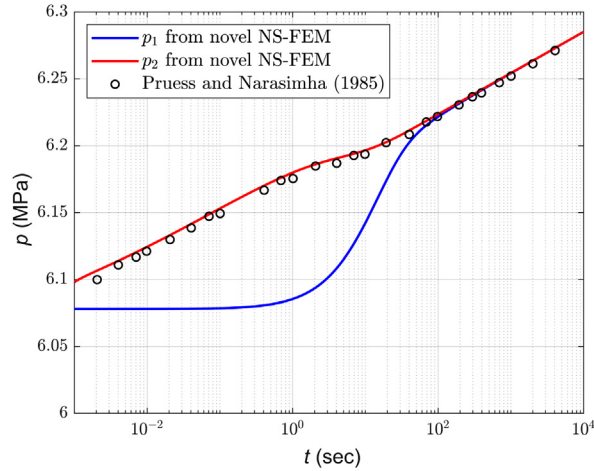


**Fig. 5.** Transient pressure responses at the wellbore ( $r = r_w$ ) for fluid flow in a naturally fractured reservoir.

#### 5.4. Homogeneous rectangular block of Tournemire shale

For the last verification example, the compression of the homogeneous rectangular block of Tournemire shale [87] is simulated, in order to illustrate the capability of the proposed numerical scheme in handling complex constitutive models. Due to the existence of the bedding plane, the anisotropy would play an important role in the solid constitutive model. Semnani et al. [88] developed a novel anisotropic version of the modified Cam–Clay model, which is abbreviated as the AMCC model for subsequent descriptions. The salient features of this AMCC model are the construction of the fourth-order projection tensor  $\mathbb{P}$  from the bedding plane orientation and application of the yield function in the projected effective stress space  $\sigma''_p = \mathbb{P} : \sigma''$ . In Zhao et al. [87], the authors have calibrated the mechanical parameters with the triaxial test data of Tournemire shale [89]. By using the calibrated parameters, they have run several boundary-value problems to highlight the dependence of the failure pattern on the bedding plane orientation  $\theta$  ( $\theta = 0$  corresponds to a horizontal bedding plane, whereas  $\theta = \pi/2$  corresponds to a vertical bedding plane, counterclockwise is positive). In this study, the aim is to reproduce these results by using the NS-FEM with modified nodal integration. It is worth mentioning that in AMCC model, the fourth-order elastic moduli tensor is not pressure ( $p'' = \sigma''_{ii}/3$ ) dependent [87], which makes it more suitable to simulate the behavior of some rocks

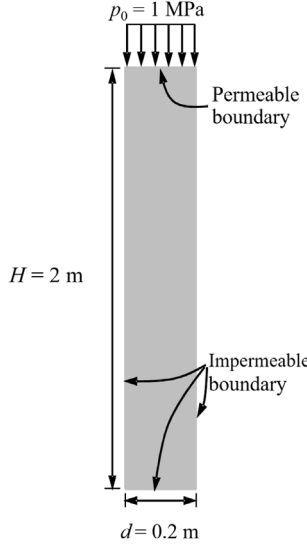


**Fig. 6.** Schematics of the 1D consolidation problem. The gray region represents a double porosity medium. The bottom edge corresponds to  $x = 0$  and the top edge corresponds to  $x = 2$  m. The mesh size is 0.02 m.

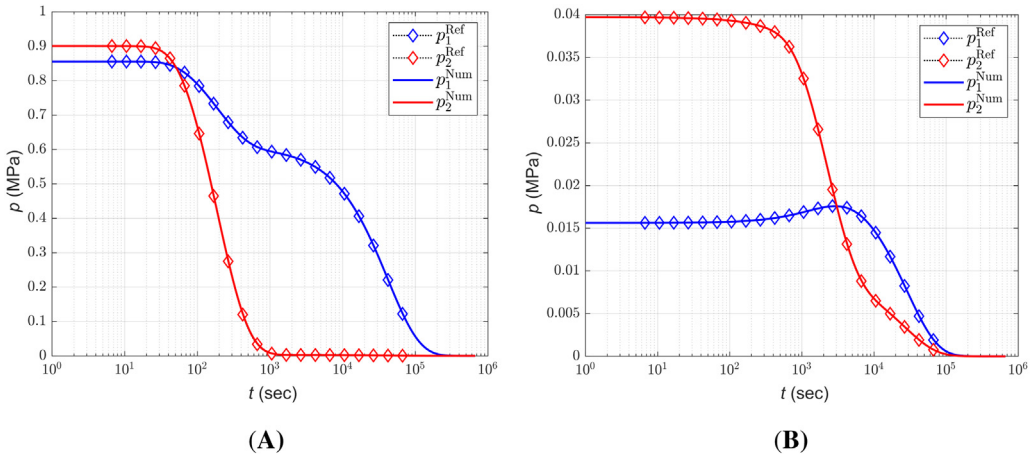


**Fig. 7. A.** Pressure responses at the bottom ( $x = 0$ ) for Case 1. **B.** Pressure responses at the bottom ( $x = 0$ ) for Case 2.

such as shale, and this assumption also relieves the effort in the implementation of the  $\mathcal{K}_u^{\text{MNI}}$  in Eq. (43). Ip and Borja [90] extended AMCC model to the unsaturated range, and they have calibrated the material parameters with another set of test data of Tournemire shale that includes degree of saturation [91].

The boundary-value problem (plane strain) considers a rectangular block of overconsolidated Tournemire shale 75 mm tall and 37.5 mm wide, with a uniform mesh size of 1.875 mm. The sample is subjected to an initial confining pressure of 1 MPa at an initial preconsolidation pressure of 40 MPa, i.e.,  $\sigma_x^0 = \sigma_y^0 = \sigma_z^0 = -1$  MPa and  $p_c^0 = -40$  MPa. The material parameters for this shale are given as  $\lambda^e = 4270$  MPa,  $a^e = -1870$  MPa,  $b^e = 5420$  MPa,  $\mu_T = 9360$  MPa,  $\mu_L = 6510$  MPa,  $c_1^p = 0.7$ ,  $c_2^p = -0.36$ ,  $c_3^p = 0.6$ ,  $M = 1.07$ ,  $\lambda^p = -0.0026$ ,  $\varepsilon_s = 1$ . Physical meanings of these parameters are given in both Zhao et al. [87] and Zhang [28]. Since this is a pure solid phase deformation problem, the fluid-related parameters are not given. The top and bottom faces are clamped so that the sample is forced to remain vertically through the loading process. The simulation result and the reference result from Zhao et al. [87] are compared in Fig. 9. Note that since the initial stress, loading scheme, and amount of compression are not reported in Zhao et al. [87], the comparison may not be perfect. Nevertheless, we can clearly observe the zone of localized plastic deformation that runs approximately parallel to the bedding

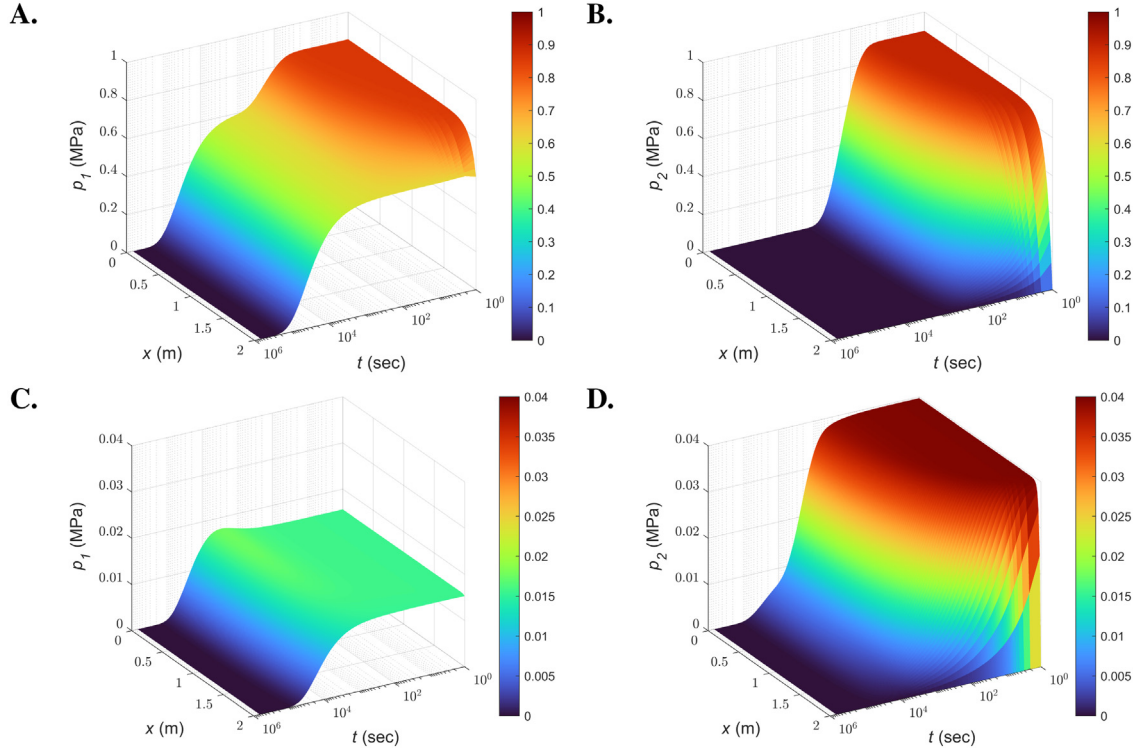


**Fig. 8.** **A.** Spatial  $p_1$  along the  $x$ -axis as a function of time in Case 1. **B.** Spatial  $p_2$  along the  $x$ -axis as a function of time in Case 1. **C.** Spatial  $p_1$  along the  $x$ -axis as a function of time in Case 2. **D.** Spatial  $p_2$  along the  $x$ -axis as a function of time in Case 2.

**Table 6**

Material parameters used in the 1D consolidation of a double porosity medium [29]. The first two parameters are used to construct  $\mathbb{C}^e$ . For modified NI,  $\varepsilon_s = \varepsilon_f = 1$ ; while for PPP,  $\tau = 2$  and  $\bar{G} = G$ .

Parameter	Case 1	Case 2
Bulk modulus $K$ (GPa)	0.6	
Shear modulus $G$ (GPa)	0.45	
Volume fraction $v^{[1]}, v^{[2]}$	0.95, 0.05	
Biot tensor $\alpha_1$ in vector form	$[0.5007, 0.5007, 0]^T$	
Biot tensor $\alpha_2$ in vector form	$[0.4775, 0.4775, 0]^T$	
Storage coefficient $A_{11}$ (GPa $^{-1}$ )	0.4825	27.0062
Storage coefficient $A_{22}$ (GPa $^{-1}$ )	0.4357	9.9085
Storage coefficient $A_{12}$ (GPa $^{-1}$ )	-0.39289	
Isotropic scalar permeability $k_1$ (m $^2$ )	0	
Isotropic scalar permeability $k_2$ (m $^2$ )	$5 \times 10^{-15}$	
Fluid viscosity $\mu_f$ (cP)	1	
Leakage parameter $\gamma$ (GPa $^{-1} \cdot s^{-1}$ )	$1.67 \times 10^{-5}$	$1.67 \times 10^{-3}$

plane for  $\theta = \pi/4$  (SD mode [28]), while it runs nearly perpendicular to the bedding plane for  $\theta = \pi/12$  (SM mode [28]). The former case may lead to the zigzag pattern in the real situation since the local bifurcation always runs in the weaker bed-normal direction [87,88] and plastic sliding failure mode along the weak planes could also occur, which is controlled by the Mohr–Coulomb friction law [92].

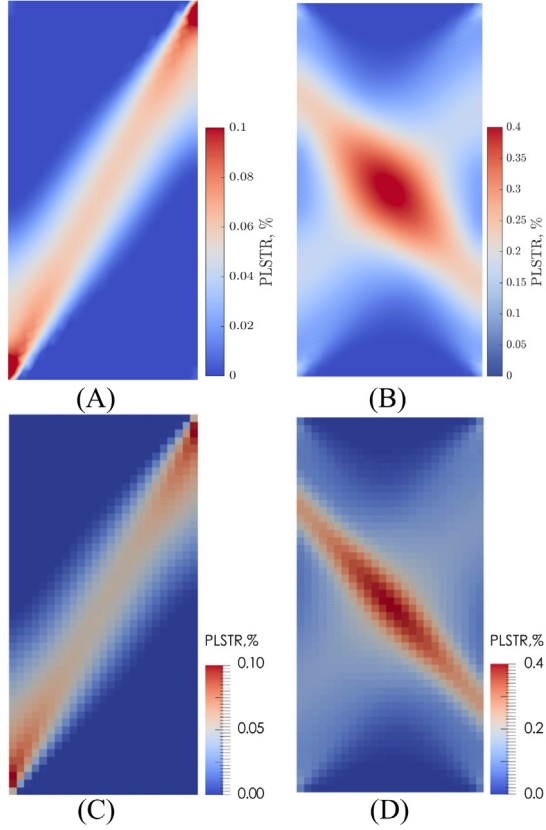


**Fig. 9.** Contours of plastic strain norm  $\|\mathbf{e}_p\|_F = \sqrt{\mathbf{e}_p : \mathbf{e}_p}$  for plane strain compression of transversely isotropic rock with clamped end. (A) Shear band for  $\theta = \pi/4$  from the proposed approach, total vertical compression is 0.098 mm completed in 49 uniform steps; (B) Shear band for  $\theta = \pi/12$  from the proposed approach, total vertical compression is 0.18 mm completed in 45 uniform steps; (C) Reference result for  $\theta = \pi/4$ ; (D) Reference result for  $\theta = \pi/12$ . The comparison may not be very accurate since the initial stress, loading scheme, and amount of compression are not reported in Zhao et al. [87].

## 6. Numerical examples

### 6.1. Shear band with permeability anisotropy

We consider in this section the boundary-value problem of an unconfined plane strain compression test. The specimen measures 0.14 m tall and 0.04 m wide. Fig. 10 presents schematics of this specimen along with the boundary conditions. The bottom edge is clamped, and the top edge is supported by vertical rollers with prescribed vertical displacement at a constant rate  $\tilde{v}$ . Note the top surface is still traction-free in the horizontal direction, *i.e.*, it could slide in the  $x$  direction. The assumed material parameters, reported in Table 7, can be realistically considered as characterizing a sample clay saturated with water [93]. In this example, the solid is simulated using a strain-softening associated Drucker–Prager model whose return mapping algorithm is given in Appendix C. In this model, the friction angle  $\phi$ , dilatancy angle  $\psi$ , and cohesion  $c$  would decay with the accumulation of plastic strain, which is given by the following equations

$$\phi = \psi = \phi_r + (\phi_p - \phi_r) \exp(-\eta \varepsilon_{eq}^p), \quad (52)$$

$$c = c_r + (c_p - c_r) \exp(-\eta \varepsilon_{eq}^p), \quad (53)$$

where  $c_p$  and  $c_r$  are the peak and residual values of cohesion,  $\phi_p$  and  $\phi_r$  are the peak and residual values of friction angle,  $\eta$  is the decay factor that controls the strain-softening rate, and  $\varepsilon_{eq}^p$  is the equivalent (deviatoric) plastic strain

**Table 7**

Material parameters used in the first example. For modified NI,  $\varepsilon_s = \varepsilon_f = 1$ ; while for PPP,  $\tau = 2$  and  $\bar{G} = G$ . Two additional cases are also considered in this example, one without fluid (pure solid phase deformation), and the other one changes  $k_2$  to be isotropic ( $10^{-16}$  m $^2$ ).

Parameter	Value
Bulk modulus $K$ (MPa)	25/3
Shear modulus $G$ (MPa)	50/13
Cohesion $c_p, c_r$ (kPa)	25, 5
Friction angle $\phi_p, \phi_r$ (rad)	$\pi/12, \pi/60$
Decay factor $\eta$	50
Volume fraction $v^{[1]}, v^{[2]}$	0.95, 0.05
Biot tensor $\alpha_1$	$v^{[1]} \mathbf{1}$
Biot tensor $\alpha_2$	$v^{[2]} \mathbf{1}$
Storage coefficient $A_{11}$ (MPa $^{-1}$ )	$(v^{[1]} v^{[2]}) / K$
Storage coefficient $A_{22}$ (MPa $^{-1}$ )	$A_{11}$
Storage coefficient $A_{12}$ (MPa $^{-1}$ )	$-A_{11}$
Isotropic scalar permeability $k_1$ (m $^2$ )	$10^{-18}$
Permeability tensor $\mathbf{k}_2(x, y, xy)$ (m $^2$ )	$(2, 1, 0.75) \times 10^{-16}$
Fluid viscosity $\mu_f$ (cP)	1
Leakage parameter $\gamma$ (MPa $^{-1} \cdot s^{-1}$ )	$2 \times 10^{-6}$
Vertical compression rate $\dot{v}$ (m/s)	$4 \times 10^{-6}$

Drainage boundary ( $p_1 = p_2 = 0$ )

Vertical Displacement control

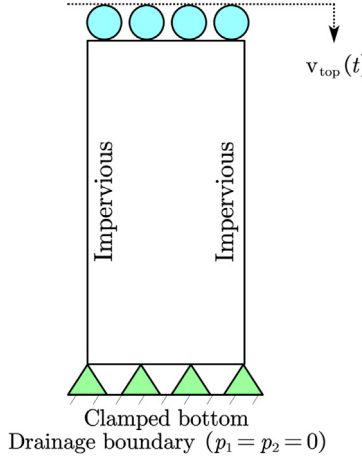


**Fig. 10.** Schematics of the unconfined plane strain compression test: the geometry, boundary, and loading conditions. The mesh size is 0.002 m.

obtained from the deviatoric plastic strain tensor  $\mathbf{e}_p^{\text{dev}}$  as

$$\text{d}\varepsilon_{eq}^p = \sqrt{\frac{2}{3} (\text{d}\mathbf{e}_p^{\text{dev}}) : (\text{d}\mathbf{e}_p^{\text{dev}})}. \quad (54)$$

The simulation runs for 25 uniform time steps with  $\Delta t = 40$  s.

We first show the distribution of  $A_{ij}$  by using Eq. (32). For elastic deformation,  $A_{ij}/(v^{[1]} v^{[2]})$  would take the value of 0.12. As seen from Fig. 11, even in the plastic deformation range,  $A_{ij}/(v^{[1]} v^{[2]})$  is still less than 0.122 for most parts, with only a few tiny regions in zigzag pattern exhibit extreme values up to 0.127. Therefore, the constant approximation of  $A_{ij}$  in Section 2.4 is feasible. Secondly, Fig. 12 presents the localized zones of deformation that develop in three samples on the deformed domain. In the case of hydromechanical coupling, the zone of localized deformation occurs in an asymmetric pattern due to the anisotropic  $\mathbf{k}_2$ , the whole sample also slides to the right

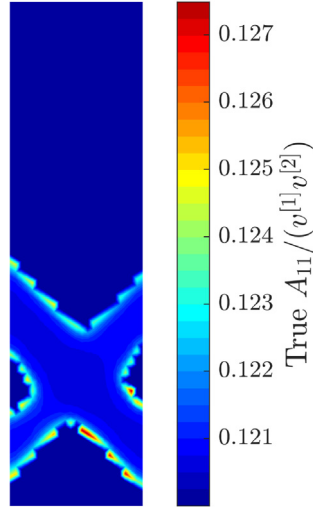


**Fig. 11.** The actual distribution of  $A_{ij}$  (MPa $^{-1}$ ) on the computational domain by using Eq. (32) from hydromechanical coupled analysis ( $t = 1000$  s). The zigzag pattern is purely a numerical result adopting the algorithmic consistent tangent operator in the return mapping algorithm [60].

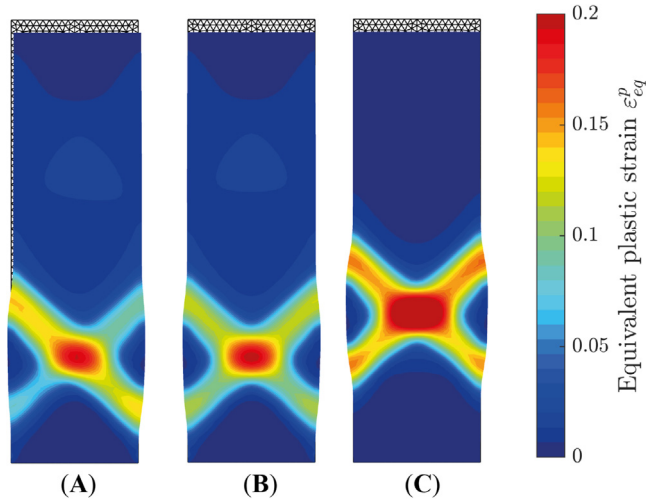


**Fig. 12.** Contours of equivalent (deviatoric) plastic strain  $\varepsilon_{eq}^p$  at  $t = 1000$  s from (A) hydromechanical coupled analysis for anisotropic  $k_2$ ; (B) hydromechanical coupled analysis for isotropic  $k_2 (10^{-16} \text{ m}^2)$ ; (C) uncoupled analysis (pure solid phase deformation).

in Fig. 12A. The location of the intersection of two conjugate shear bands gets lower in Fig. 12A and Fig. 12B, compared with Fig. 12C, due to the presence of fluid pressure. For pure solid phase deformation, there might be more compaction within the zone of localized deformation, as Fig. 12C has the largest value of  $\varepsilon_{eq}^p$ . Lastly, the contours of  $p_1$  and  $p_2$  from the last time step are plotted in Fig. 13. Similarities between the  $\varepsilon_{eq}^p$  and pore pressure contours are clearly observed for the field of  $p_1$  [90], while the contours of  $p_2$  are almost (tilted) straight lines except for the zone of localized deformation and drainage boundary.

## 6.2. Rigid footing penetration on an unsupported double porosity medium

The second example analyzes the plane strain problem of rigid foundation on a vertical cut [93]. To simplify the problem, the contact between the rigid foundation and porous medium is assumed to be perfectly coherent. In other words, the rigid footing penetration could be treated as an inhomogeneous Dirichlet boundary condition

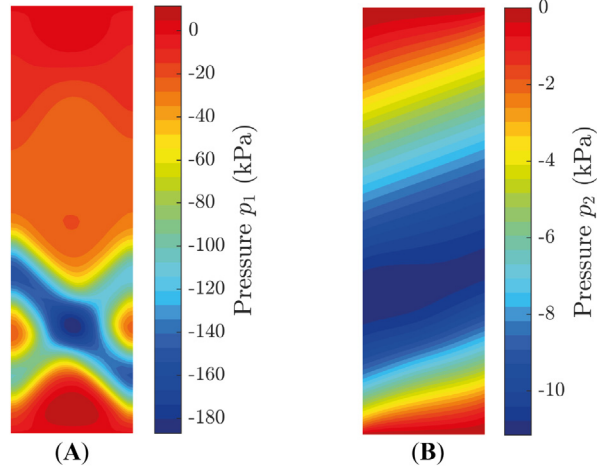


**Fig. 13.** **A.** Contours of  $p_1$  at  $t = 1000$  s for anisotropic  $k_2$ . **B.** Contours of  $p_2$  at  $t = 1000$  s for anisotropic  $k_2$ .

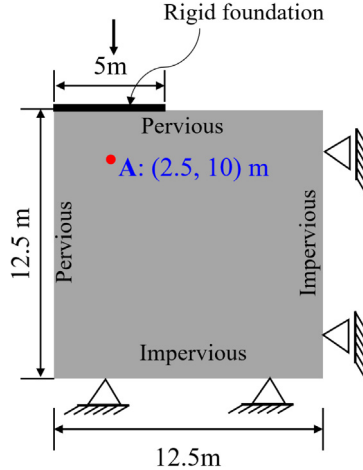


**Fig. 14.** Schematics of the rigid footing penetration problem: the geometry, boundary, and loading conditions. The origin  $(0, 0)$  coincides with the lower-left corner of the domain. The mesh size is 0.25 m.

on the corresponding boundary. Geometry and boundary conditions are presented in Fig. 14, which are the same as those in Callari and Armero [93]. The same solid constitutive model used in Section 6.1 is adopted here. The demonstration of the performance and necessity of the additional correction terms with superscripts “MNI” and “STAB” in Section 4 are shown first. In order to highlight the importance of these terms, the fundamental single porosity case [33] is simulated with the material parameters shown in Table 8. To examine the effectiveness of modified nodal integration,  $\varepsilon_f = \varepsilon_s$  are changed from 1 to 0, and a total vertical displacement of 0.25 m is applied within a period of 1000 s by 5 uniform steps. The results from the last time step ( $t = 1000$  s) are compared in Fig. 15. It can be seen that the modified nodal integration could eliminate the noisy zigzag pattern in both displacement and pore pressure contours. Next, to further examine the effectiveness of PPP technique in the nearly undrained condition [34],  $\tau$  is changed from 2 to 0, all the boundaries are impermeable, and an indentation of 0.2 m happens in  $\Delta t = 10^{-5}$  s. The simulation just runs for one time step and results are compared in Fig. 16. An evident checkerboard pattern can be largely alleviated to a reasonable mode when considering the PPP term. Therefore, it is concluded that both modified nodal integration and PPP technique are necessary in this problem with material non-linearity by using NS-FEM.

The parametric analysis is performed next. The material parameters for four different cases are summarized in Table 9. Fig. 17 depicts the distribution of equivalent (deviatoric) plastic strain  $\varepsilon_{eq}^p$  at the vertical penetration

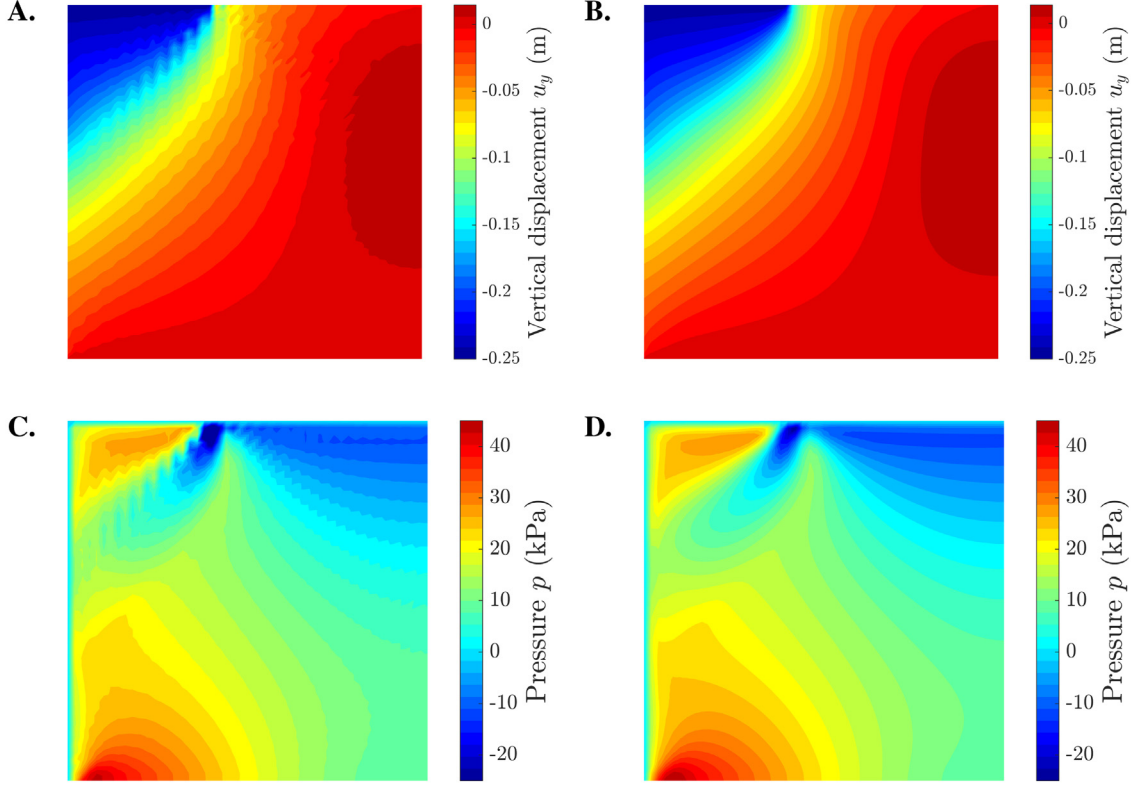


**Fig. 15.** **A.** Contours of vertical displacement with  $\varepsilon_s = \varepsilon_f = 0$ . **B.** Contours of vertical displacement with  $\varepsilon_s = \varepsilon_f = 1$ . **C.** Contours of pore pressure with  $\varepsilon_s = \varepsilon_f = 0$ . **D.** Contours of pore pressure with  $\varepsilon_s = \varepsilon_f = 1$ .

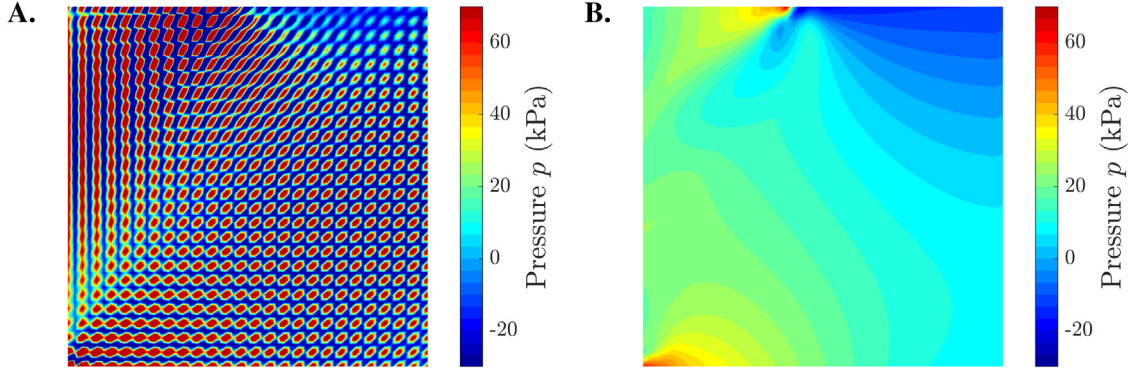


**Fig. 16.** **A.** Contours of pore pressure in the undrained limit with  $\tau = 0$ . **B.** Contours of pore pressure in the undrained limit with  $\tau = 2$ .

of 0.5 m. A clear shear band is formed in the strain-softening material (Case 1), indicating the localized failure feature. On the contrary, if there is no strain-softening, the  $\varepsilon_{eq}^p$  exhibits a bulb shape around the right end of the rigid foundation. Similar result is also obtained by using the Mohr–Coulomb model in Wang et al. [33]. For Case 1 and Case 4, the contours of  $p_1$  and  $p_2$  are plotted in Figs. 18 and 19. Similar to the findings in Section 6.1, in this example, the patterns of  $p_1$  and  $\varepsilon_{eq}^p$  are also alike. For  $p_2$ , as seen from Fig. 18B, its pattern is controlled by both the shear band direction and principal directions of the anisotropic  $\mathbf{k}_2$ . The pore pressures reported in Fig. 20 are calculated at point A under the foundation center (see Fig. 14). The curves of  $p_1$  for Cases 1–3 match well with that in Callari and Armero [93] in a qualitative manner. For a much smaller  $\mathbf{k}_2$  (Case 2), the calculated  $p_1$  and  $p_2$

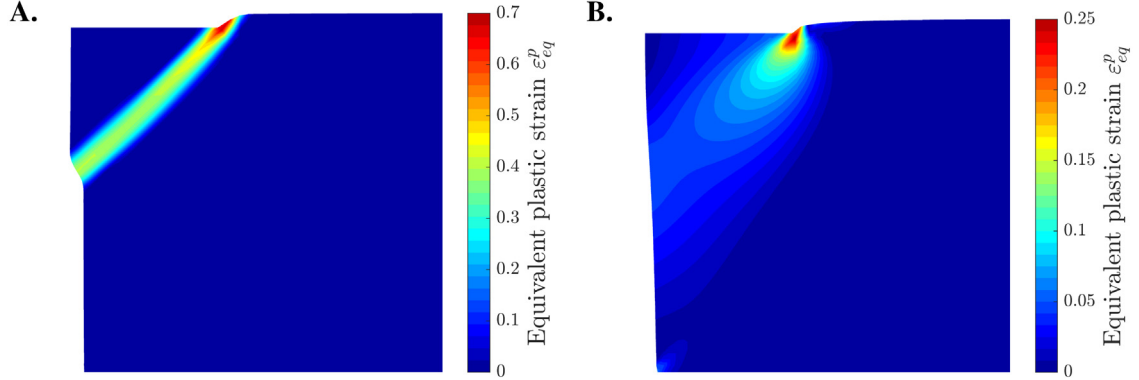


**Fig. 17.** **A.** Contours of equivalent (deviatoric) plastic strain  $\varepsilon_{eq}^p$  in Case 1 at  $t = 1000$  s on the deformed domain. **B.** Contours of equivalent (deviatoric) plastic strain  $\varepsilon_{eq}^p$  in Case 4 at  $t = 1000$  s on the deformed domain.

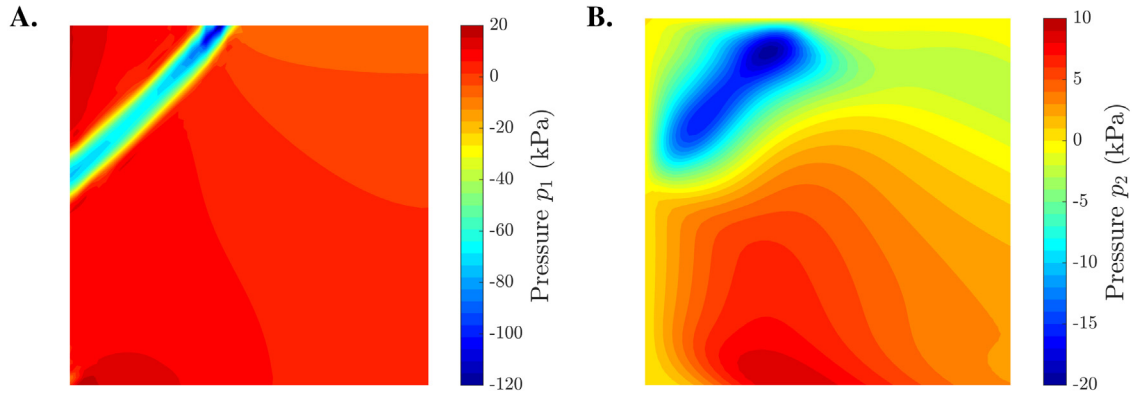


**Fig. 18.** **A.** Contours of  $p_1$  in Case 1 at  $t = 1000$  s. **B.** Contours of  $p_2$  in Case 1 at  $t = 1000$  s.

are fairly close to each other [59]. Furthermore, for a much slower penetration rate as in Case 3, the fluctuation of  $p_2$  almost disappears while it has a minor impact on  $p_1$ . This unique feature of double porosity media is different from that in Callari and Armero [93] for single porosity media.

## 7. Closure

Geomaterials are generally anisotropic, inelastic, and could contain multi-scale pore spaces. In this work, a new poroelastoplastic formulation for anisotropic double porosity media is derived. The formulation takes the properties of intrinsic single porosity constituents into consideration, which could capture the additional physics, namely, the anisotropy of each material. To solve the initial-boundary-value problem of double porosity media, a novel fully coupled stabilized node-based smoothed FEM adopting 3-node linear triangular element has been proposed. Effective correction terms for direct nodal integration and Babuška–Brezzi restriction are also implemented. The spatial discretization follows the standard mixed FEM formulation and the temporal discretization adopts a Backward Euler implicit scheme.

Four benchmark tests were conducted that cover a wide range of engineering science, and the results of the proposed stabilized NS-FEM agreed well with all previous reference solutions. For the applications, symmetric and asymmetric conjugate shear bands in a laboratory specimen, and localized and inclined patterns of pore pressures

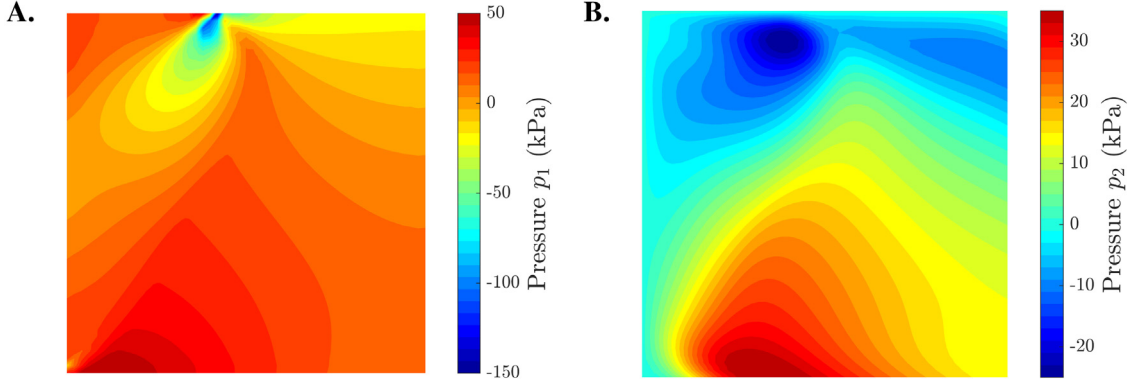


**Fig. 19.** **A.** Contours of  $p_1$  in Case 4 at  $t = 1000$  s. **B.** Contours of  $p_2$  in Case 4 at  $t = 1000$  s.

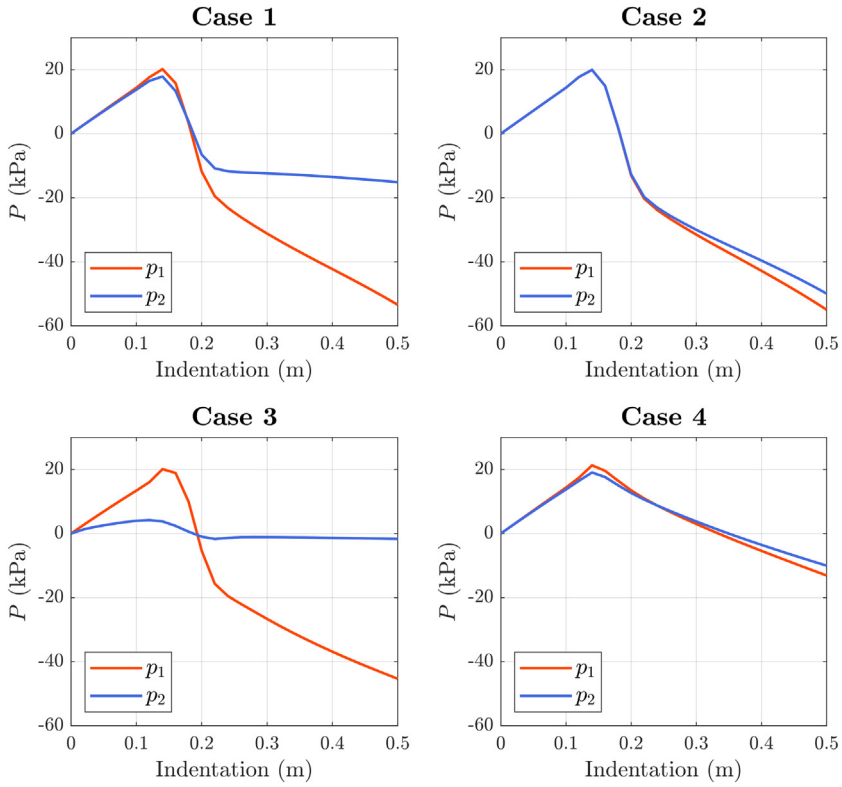


**Fig. 20.** Pore pressure results at point A obtained from four different cases.

could be obtained, showing the strength of this proposed framework. The numerical evidence of constant storage coefficients is also provided. The abilities of modified nodal integration and PPP terms were demonstrated in the rigid footing penetration problem. A clear shear band for the strain-softening soil could also be observed.

Future work will focus on the 3D extension of this approach along with more complex geotechnical practices, while at the same time, combination with discrete fracture mechanics [79,94,95] will definitely provide more interesting and practical results for engineering.

**Table 8**

Material parameters used in the second example for highlighting the contributions of  $\varepsilon_s$ ,  $\varepsilon_f$ , and  $\tau$ . Note that  $\bar{G} = G$  always holds in this example and the value of  $\gamma$  will not affect the result.

Parameter	Value
Bulk modulus $K$ (MPa)	5/3
Shear modulus $G$ (MPa)	10/13
Cohesion $c$ (kPa)	25
Friction angle $\phi$ (rad)	$\pi/12$
Volume fraction $v^{[1]}, v^{[2]}$	0.5, 0.5
Biot tensor $\alpha_1$	$v^{[1]} \mathbf{1}$
Biot tensor $\alpha_2$	$v^{[2]} \mathbf{1}$
Storage coefficient $A_{11}$ (MPa $^{-1}$ )	$(v^{[1]} v^{[2]}) / K$
Storage coefficient $A_{22}$ (MPa $^{-1}$ )	$A_{11}$
Storage coefficient $A_{12}$ (MPa $^{-1}$ )	$-A_{11}$
Isotropic scalar permeability $k_1$ (m $^2$ )	$10^{-14}$
Isotropic scalar permeability $k_2$ (m $^2$ )	$10^{-14}$
Fluid viscosity $\mu_f$ (cP)	1
Leakage parameter $\gamma$ (MPa $^{-1} \cdot s^{-1}$ )	$2 \times 10^{-6}$
Default $\varepsilon_s, \varepsilon_f$	1
Default $\tau$	2

**Table 9**

Material parameters used in the second example for parametric analysis of a double porosity medium. All the boundaries are impermeable for  $p_1$ . For modified NI,  $\varepsilon_s = \varepsilon_f = 1$ ; while for PPP,  $\tau = 2$  and  $\bar{G} = G$ . Three additional cases are also considered in this example. For Case 2, the  $k_2$  is scaled by a factor of 0.01. For Case 3, the time step size is increased to 4000 s, which implies the vertical penetration rate  $\tilde{v}$  is decreased to  $5 \times 10^{-6}$  m/s. For Case 4,  $\eta$  is set to 0, which implies that there is no strain-softening.

Parameter	Value (Case 1)
Bulk modulus $K$ (MPa)	5/3
Shear modulus $G$ (MPa)	10/13
Cohesion $c_p, c_r$ (kPa)	25, 5
Friction angle $\phi_p, \phi_r$ (rad)	$\pi/12, \pi/60$
Decay factor $\eta$	50
Volume fraction $v^{[1]}, v^{[2]}$	0.95, 0.05
Biot tensor $\alpha_1$	$v^{[1]} \mathbf{1}$
Biot tensor $\alpha_2$	$v^{[2]} \mathbf{1}$
Storage coefficient $A_{11}$ (MPa $^{-1}$ )	$(v^{[1]} v^{[2]}) / K$
Storage coefficient $A_{22}$ (MPa $^{-1}$ )	$A_{11}$
Storage coefficient $A_{12}$ (MPa $^{-1}$ )	$-A_{11}$
Isotropic scalar permeability $k_1$ (m $^2$ )	$10^{-18}$
Permeability tensor $k_2(xx, yy, xy)$ (m $^2$ )	$(7.5, 2.5, -4) \times 10^{-14}$
Fluid viscosity $\mu_f$ (cP)	1
Leakage parameter $\gamma$ (MPa $^{-1} \cdot s^{-1}$ )	$2 \times 10^{-6}$
Vertical penetration rate $\tilde{v}$ (m/s)	$5 \times 10^{-4}$
Number of uniform time steps	25
Time step size $\Delta t$ (s)	40

## Declaration of competing interest

The authors declare that they have no known competing financial interests or personal relationships that could have appeared to influence the work reported in this paper.

## Data availability

Data will be made available on request. Supplementary material related to this article can be found at <https://github.com/qizhang94/GEOKEYFEM.HM> under the **Releases** menu. Please remember to cite the corresponding paper if you use any of these codes for research or industrial purposes.

## Acknowledgments

This research is financially supported by The Hong Kong Polytechnic University Strategic Importance Fund (ZE2T) and Project of Research Institute of Land and Space (CD78).

## Appendix A. Multiple porosity media

In the multiple porosity media,  $N$  materials (constituents) are characterized by  $v^{[l]}$ ,  $\mathbb{S}^{[l]}$ ,  $\mathbf{B}^{[l]}$ ,  $\boldsymbol{\alpha}^{[l]}$ , and  $D^{[l]}$  ( $l = 1, 2, \dots, N$ ). They are assumed to be anisotropic in the most general case. The macroscopic poroelastic equation for the whole mixture is simply a natural extension of Eq. (12), which may be written as

$$\begin{bmatrix} \mathbf{Vec}(\boldsymbol{\epsilon}) \\ \zeta_1 \\ \vdots \\ \zeta_N \end{bmatrix} = \begin{bmatrix} \mathbf{Mat}(\mathbb{S}^*) & a_1 & \cdots & a_N \\ a_1^T & d_{11} & \cdots & d_{1N} \\ \vdots & \vdots & \ddots & \vdots \\ a_N^T & d_{N1} & \cdots & d_{NN} \end{bmatrix} \begin{bmatrix} \mathbf{Vec}(\boldsymbol{\sigma}) \\ p_1 \\ \vdots \\ p_N \end{bmatrix}. \quad (\text{A.1})$$

The same strain compatibility relation  $\mathbf{Vec}(\boldsymbol{\epsilon}) = \sum_{k=1}^N v^{[k]} \mathbf{Vec}(\boldsymbol{\epsilon}^{[k]})$  and the uniform confining stress condition are applied next, in order to derive the coefficients in Eq. (A.1). The results read ( $l = 1, 2, \dots, N$ )

$$\mathbf{Mat}(\mathbb{S}^*) = \sum_{k=1}^N v^{[k]} \mathbf{Mat}(\mathbb{S}^{[k]}), \quad (\text{A.2})$$

$$a_l = \frac{1}{3} v^{[l]} D^{[l]} \mathbf{Vec}(\mathbf{B}^{[l]}), \quad (\text{A.3})$$

$$d_{ll} = v^{[l]} D^{[l]}. \quad (\text{A.4})$$

Note all the off-diagonal terms  $d_{ij}$  ( $i \neq j$ ) are zero [25]. Eq. (A.1) can be rewritten in the mixed stiffness form by exchanging the position of  $\boldsymbol{\epsilon}$  and  $\boldsymbol{\sigma}$ , which would give the familiar Biot tensors and storage coefficients. The pure stiffness form is obtained by inverting the matrix in Eq. (A.1).

We want to add a further remark about the strain compatibility relation and the uniform confining stress condition. These two conditions can be visually obtained from the equivalence of the potential energy density [96]. In other words, the energy density of the multiple porosity material  $U$  must be equal to the weighted sum of the individual constituents' energy density  $U_i$ . This can be expressed mathematically as

$$U = \sum_{i=1}^N v^{[i]} U_i, \quad (\text{A.5})$$

$$U = \frac{1}{2} \left( \boldsymbol{\sigma} : \boldsymbol{\epsilon} + \sum_{i=1}^N \zeta_i p_i \right), \quad (\text{A.6})$$

$$U_i = \frac{1}{2} (\boldsymbol{\sigma}^{[i]} : \boldsymbol{\epsilon}^{[i]} + \bar{\zeta}_i p_i). \quad (\text{A.7})$$

Note that  $\zeta_i = v^{[i]} \bar{\zeta}_i$  in which  $\zeta_i$  represents the global fluid content variation and  $\bar{\zeta}_i$  represents the local fluid content variation.

## Appendix B. Quantitative analysis of the momentum supply generated from mass transfer

Through this appendix, we compare the order of magnitude between the momentum supply generated from mass transfer and body force due to pressure coupling. To be more specific, the inter-continuum momentum transfer is given by [14,59,64]

$$\tilde{\Gamma} = \rho_f \gamma (p_1 - p_2) (\mathbf{v}_2 - \mathbf{v}_1), \quad (\text{B.1})$$

where  $\mathbf{v}_1$  and  $\mathbf{v}_2$  are the interstitial fluid velocities within two materials,  $\gamma$  is a leakage parameter, and  $\rho_f$  is the fluid density. The body force term is  $\nabla p_2$ . Even though both  $\tilde{\Gamma}$  and  $\nabla p_2$  are from the deformation equation, they actually reflect the impact of fluid flow on the solid deformation. For  $\mathbf{v}_2$ , it is related to  $\nabla p_2$  through Darcy's law and definition of Darcy velocity  $\mathbf{q}_2$ . The  $\mathbf{q}_2$  is the average of relative velocity  $\mathbf{v}_2 - \mathbf{v}_s$  over the whole crossing area, where  $\mathbf{v}_s$  is the velocity of the solid. By using the mixture theory [21,97], the area fraction is equal to the volume fraction, thus  $\mathbf{q}_2 = v^{[2]} \phi^{[2]} (\mathbf{v}_2 - \mathbf{v}_s) = \phi_2 (\mathbf{v}_2 - \mathbf{v}_s)$ . Similarly,  $\mathbf{q}_1 = v^{[1]} \phi^{[1]} (\mathbf{v}_1 - \mathbf{v}_s) = \phi_1 (\mathbf{v}_1 - \mathbf{v}_s)$ . By using the fact that  $\|\mathbf{q}_1\|_2 \ll \|\mathbf{q}_2\|_2$ , the quantitative comparison between  $\tilde{\Gamma}$  and  $\nabla p_2$  could further be simplified to the calculation of the following dimensionless number  $N_D$  and check whether it is way less than 1

$$N_D = \rho_f \gamma |p_1 - p_2| \frac{k_2}{\mu_f \phi_2}. \quad (\text{B.2})$$

Here all the quantities should be understood as the characteristic quantities that can be estimated from relevant published results.

We first use the result from Zhao and Borja [18]. From their Table 2, the fluid density  $\rho_f$  takes the value of 1 ton/m<sup>3</sup>, which is a common value for water.  $\gamma$  is evaluated by  $\gamma = \bar{k} \bar{\alpha} / \mu_f$ , where  $\bar{k} = 1$  nD,  $\bar{\alpha} = 10$  m<sup>-2</sup>, and  $\mu_f = 1$  cP. The porosity  $\phi_2$  is the  $\phi^M$  in Zhao and Borja [18], which takes the value of 0.1. A proper characteristic value of  $k_2$  is 1  $\mu$ D, i.e., the permeability  $\kappa_{\parallel}$  parallel to bedding in Zhao and Borja [18]. From the numerical simulation result Fig. 8 of Zhao and Borja [18], an reasonable estimate of  $|p_1 - p_2|$  is 1 MPa. Using these numbers,  $N_D$  is  $9.7402 \times 10^{-23}$ , which suggests that as long as the surface load magnitude is realistic, the term  $\tilde{\Gamma}$  could always be ignored in balance of linear momentum equation.

Above analysis is for a typical example in geotechnical engineering. Now  $N_D$  is calculated for a naturally fractured reservoir [84]. To do so,  $N_D$  is rewritten in terms of dimensionless pressures  $p_{D1}$  and  $p_{D2}$  [84], which is given as

$$N_D = \rho_f \gamma (p_{D2} - p_{D1}) \frac{QB_o}{2\pi H \phi_2}, \quad (\text{B.3})$$

where  $Q$  is the volumetric flow rate,  $B_o$  is the formation volume factor, and  $H$  is the reservoir thickness. From Figs. 2, 3, 4, 5 in Zhang et al. [84], a conservative estimate of  $p_{D2} - p_{D1}$  under feasible ranges of  $\omega$ ,  $\lambda$ , and  $r_{De}$  is 10. For an oil reservoir, it is assumed that  $\rho_f = 850$  kg/m<sup>3</sup>,  $\mu_f = 0.009$  Pa · s, and matrix permeability  $k_1 = 1$  mD [98]. For  $Q$ ,  $B_o$ , and  $H$ , they take following values from Ahmed [99]:  $Q = 2554$  STB/day,  $B_o = 2.3$  bbl/STB, and  $H = 17$  ft.<sup>1</sup> To estimate  $\gamma$ , the empirical formula  $\gamma = \sigma k_1 / \mu_f$  is adopted where  $\sigma$  is the shape factor (same as  $\bar{\alpha}$  used in Zhao and Borja [18]). A typical value of  $\sigma = 0.4$  ft<sup>-2</sup> from Fig. 10 of Sarma and Aziz [98] is adopted here. Finally for  $\phi_2$ , a typical value would be  $\phi_2 = 0.001$ .<sup>2</sup> Using these numbers,  $N_D$  is  $1.3324 \times 10^{-9}$ , which is still a tiny number even under this high flow rate. Thus, it is shown that  $\tilde{\Gamma}$  is negligible with respect to other force density terms.

## Appendix C. Return mapping algorithm of the Drucker–Prager plasticity theory with softening

For simplicity,  $\sigma$  is used to represent the effective stress tensor of solid as that in solid mechanics. That is to say, please interpret it as  $\sigma''$  in the hydromechanical coupling analysis.

Step 1. Compute the following quantities ( $\|\cdot\|_F$  is the Frobenius norm)

$$\sigma^{\text{tr}} = \sigma_n + \mathbb{C}^e : \Delta e,$$

<sup>1</sup> Suppose the wellbore radius  $r_w$  is 0.375 ft [10], the seepage velocity would be 0.0029 m/s calculated from  $Q$ ,  $B_o$ ,  $H$ , and  $r_w$ , which is quite high for laminar flow.

<sup>2</sup> In fact,  $\phi^M = 0.1$  used in Zhao and Borja [18] may not be very realistic, it could be too large for a shale reservoir.

$$p^{\text{tr}} = \frac{\text{Tr}(\sigma^{\text{tr}})}{3},$$

$$\mathbf{s}^{\text{tr}} = \boldsymbol{\sigma}^{\text{tr}} - p^{\text{tr}} \mathbf{1},$$

$$q^{\text{tr}} = \sqrt{\frac{3}{2}} \|\mathbf{s}^{\text{tr}}\|_F,$$

$$\hat{\mathbf{n}} = \frac{\mathbf{s}^{\text{tr}}}{\|\mathbf{s}^{\text{tr}}\|_F}.$$

Step 2. The yield function of the Drucker–Prager plasticity is of the form

$$\tilde{f}(x, y) = \sqrt{\frac{2}{3}}y + Bx - A,$$

where  $A$  and  $B$  are two material parameters, and they are functions of cohesion  $c$  and friction angle  $\phi$ . One possible choice is by making the Drucker–Prager yield surface inscribe the Mohr–Coulomb yield surface, which yields

$$A = \frac{3\sqrt{2}c \cos \phi}{\sqrt{9 + 3 \sin^2 \phi}},$$

$$B = \frac{3\sqrt{2} \sin \phi}{\sqrt{9 + 3 \sin^2 \phi}}.$$

We also define another parameter  $b$  in an analogous manner as

$$b = \frac{3\sqrt{2} \sin \psi}{\sqrt{9 + 3 \sin^2 \psi}},$$

where  $\psi \leq \phi$  is the dilatancy angle. Now we check the sign of  $\tilde{f}(p^{\text{tr}}, q^{\text{tr}})$ . For a positive number, we would proceed to step 3. Otherwise, the final stress  $\boldsymbol{\sigma} = \boldsymbol{\sigma}^{\text{tr}}$  and algorithm is terminated ( $c$  and  $\phi$  remain the same, the algorithmic stress–strain tangent operator is  $\mathbb{C}^e$ ).

Step 3. Calculate the discrete plastic multiplier  $\Delta\lambda$  as [60]

$$\Delta\lambda = \frac{\sqrt{2/3}q^{\text{tr}} + Bp^{\text{tr}} - A}{2G + BKb},$$

where  $K$  is the bulk modulus and  $G$  is the shear modulus used to construct  $\mathbb{C}^e$ . Note that this equation for  $\Delta\lambda$  is only correct for isotropic elastoplasticity. For anisotropic elastoplasticity, a closed-form solution of  $\Delta\lambda$  [28] may not be easy to obtain.

Step 4. Compute the final stress  $\boldsymbol{\sigma}$  and update  $c$ ,  $\phi$ , and  $\psi$  (or equivalently:  $A$ ,  $B$ , and  $b$ ) by using the softening law Eqs. (52)(53) according to the new equivalent (deviatoric) plastic strain  $\varepsilon_{eq}^p$

$$\boldsymbol{\sigma} = \boldsymbol{\sigma}^{\text{tr}} - \Delta\lambda(Kb\mathbf{1} + 2G\hat{\mathbf{n}}),$$

$$\varepsilon_{eq}^p = (\varepsilon_{eq}^p)_n + \sqrt{\frac{2}{3}}\Delta\lambda.$$

The algorithmic stress–strain tangent operator is

$$\mathbb{C} = \mathbb{C}^e - (Kb\mathbf{1} + 2G\hat{\mathbf{n}}) \otimes \frac{2G\hat{\mathbf{n}} + BK\mathbf{1}}{2G + BKb} - \frac{4G^2\Delta\lambda}{\|\mathbf{s}^{\text{tr}}\|_F} \left( \mathbb{I} - \frac{1}{3}\mathbf{1} \otimes \mathbf{1} - \hat{\mathbf{n}} \otimes \hat{\mathbf{n}} \right),$$

where  $\mathbb{I}$  is the symmetric fourth-order identity tensor.

## Appendix D. Supplementary data

Supplementary material related to this article can be found online at <https://doi.org/10.1016/j.cma.2022.115666>.

## References

- [1] M. Bai, D. Elsworth, Coupled Processes in Subsurface Deformation, Flow, and Transport, American Society of Civil Engineers, Reston, VA, 2000, <http://dx.doi.org/10.1061/9780784404607>.
- [2] N. Khalili, A.P.S. Selvadurai, A fully coupled constitutive model for thermo-hydro-mechanical analysis in elastic media with double porosity, *Geophys. Res. Lett.* 30 (24) (2003) 2268, <http://dx.doi.org/10.1029/2003GL018838>.
- [3] J.G. Berryman, Extension of poroelastic analysis to double-porosity materials: New technique in microgeomechanics, *J. Eng. Mech.* 128 (8) (2002) 840–847, [http://dx.doi.org/10.1061/\(ASCE\)0733-9399\(2002\)128:8\(840\)](http://dx.doi.org/10.1061/(ASCE)0733-9399(2002)128:8(840)).
- [4] J.G. Berryman, S.R. Pride, Models for computing geomechanical constants of double-porosity materials from the constituents' properties, *J. Geophys. Res.* 107 (B3) (2002) 2052, <http://dx.doi.org/10.1029/2000JB000108>.
- [5] J.G. Berryman, H.F. Wang, The elastic coefficients of double-porosity models for fluid transport in jointed rock, *J. Geophys. Res. Solid Earth* 100 (B12) (1995) 24611–24627, <http://dx.doi.org/10.1029/95JB02161>.
- [6] H.R. Ghafouri, R.W. Lewis, A finite element double porosity model for heterogeneous deformable porous media, *Int. J. Numer. Anal. Methods Geomech.* 20 (11) (1996) 831–844.
- [7] T. Wang, P. Wang, Z.-Y. Yin, F. Zhang, DEM-DFM modeling of suffusion in calcareous sands considering the effect of double-porosity, *Comput. Geotech.* 151 (2022) 104965, <http://dx.doi.org/10.1016/j.comgeo.2022.104965>.
- [8] G.I. Barenblatt, Iu.P. Zheltov, I.N. Kochina, Basic concepts in the theory of seepage of homogeneous liquids in fissured rocks, *J. Appl. Math. Mech.* 24 (5) (1960) 1286–1303, [http://dx.doi.org/10.1016/0021-8928\(60\)90107-6](http://dx.doi.org/10.1016/0021-8928(60)90107-6).
- [9] J.E. Warren, P.J. Root, The behavior of naturally fractured reservoirs, *Soc. Petrol. Eng. J.* 3 (03) (1963) 245–255, <http://dx.doi.org/10.2118/426-PA>.
- [10] H. Kazemi, Pressure transient analysis of naturally fractured reservoirs with uniform fracture distribution, *Soc. Petrol. Eng. J.* 9 (04) (1969) 451–462, <http://dx.doi.org/10.2118/2156-A>.
- [11] H. Kazemi, L.S. Merrill, K.L. Porterfield, P.R. Zeman, Numerical simulation of water-oil flow in naturally fractured reservoirs, *Soc. Petrol. Eng. J.* 16 (06) (1976) 317–326, <http://dx.doi.org/10.2118/5719-PA>.
- [12] R.K. Wilson, E.C. Aifantis, On the theory of consolidation with double porosity, *Internat. J. Engrg. Sci.* 20 (9) (1982) 1009–1035, [http://dx.doi.org/10.1016/0020-7225\(82\)90036-2](http://dx.doi.org/10.1016/0020-7225(82)90036-2).
- [13] K.T. Lewallen, H.F. Wang, Consolidation of a double-porosity medium, *Int. J. Solids Struct.* 35 (34–35) (1998) 4845–4867, [http://dx.doi.org/10.1016/S0020-7683\(98\)00097-3](http://dx.doi.org/10.1016/S0020-7683(98)00097-3).
- [14] R.I. Borja, A. Koliji, On the effective stress in unsaturated porous continua with double porosity, *J. Mech. Phys. Solids* 57 (8) (2009) 1182–1193, <http://dx.doi.org/10.1016/j.jmps.2009.04.014>.
- [15] J. Choo, J.A. White, R.I. Borja, Hydromechanical modeling of unsaturated flow in double porosity media, *Int. J. Geomech.* 16 (6) (2016) D4016002, [http://dx.doi.org/10.1061/\(ASCE\)GM.1943-5622.0000558](http://dx.doi.org/10.1061/(ASCE)GM.1943-5622.0000558).
- [16] R.I. Borja, Cam-Clay plasticity. Part v: A mathematical framework for three-phase deformation and strain localization analyses of partially saturated porous media, *Comput. Methods Appl. Mech. Engrg.* 193 (48–51) (2004) 5301–5338, <http://dx.doi.org/10.1016/j.cma.2003.12.067>.
- [17] Q. Zhang, J. Choo, R.I. Borja, On the preferential flow patterns induced by transverse isotropy and non-Darcy flow in double porosity media, *Comput. Methods Appl. Mech. Engrg.* 353 (2019) 570–592, <http://dx.doi.org/10.1016/j.cma.2019.04.037>.
- [18] Y. Zhao, R.I. Borja, Anisotropic elastoplastic response of double-porosity media, *Comput. Methods Appl. Mech. Engrg.* 380 (2021) 113797, <http://dx.doi.org/10.1016/j.cma.2021.113797>.
- [19] A.H.D. Cheng, Poroelasticity, Springer Science+Business Media, New York, NY, 2016, <http://dx.doi.org/10.1007/978-3-319-25202-5>.
- [20] Y. Liu, R.I. Borja, Time scales in the primary and secondary compression of soils, *Int. J. Numer. Anal. Methods Geomech.* 46 (8) (2022) 1383–1408, <http://dx.doi.org/10.1002/nag.3350>.
- [21] R.I. Borja, On the mechanical energy and effective stress in saturated and unsaturated porous continua, *Int. J. Solids Struct.* 43 (6) (2006) 1764–1786, <http://dx.doi.org/10.1016/j.ijsolstr.2005.04.045>.
- [22] Q. Zhang, Strip load on transversely isotropic elastic double porosity media with strong permeability contrast, *Adv. Geo-Energy Res.* 5 (4) (2021) 353–364, <http://dx.doi.org/10.46690/ager.2021.04.02>.
- [23] Q. Zhang, R.I. Borja, Poroelastic coefficients for anisotropic single and double porosity media, *Acta Geotech.* 16 (10) (2021) 3013–3025, <http://dx.doi.org/10.1007/s11440-021-01184-y>.
- [24] R.I. Borja, J. Choo, Cam-Clay plasticity, Part VIII: A constitutive framework for porous materials with evolving internal structure, *Comput. Methods Appl. Mech. Engrg.* 309 (2016) 653–679, <http://dx.doi.org/10.1016/j.cma.2016.06.016>.
- [25] J. Kim, E.L. Sonnenthal, J. Rutqvist, Formulation and sequential numerical algorithms of coupled fluid/heat flow and geomechanics for multiple porosity materials, *Internat. J. Numer. Methods Engrg.* 92 (5) (2012) 425–456, <http://dx.doi.org/10.1002/nme.4340>.
- [26] A. Mehrabian, Y.N. Abousleiman, Generalized Biot's theory and Mandel's problem of multiple-porosity and multiple-permeability poroelasticity, *J. Geophys. Res. Solid Earth* 119 (4) (2014) 2745–2763, <http://dx.doi.org/10.1002/2013JB010602>.
- [27] P. Zheng, Z. Gao, B. Ding, The elastic coefficients of double-porosity materials: A revisit, *Transp. Porous Media* 111 (3) (2016) 555–571, <http://dx.doi.org/10.1007/s11242-015-0611-9>.
- [28] Q. Zhang, Hydromechanical modeling of solid deformation and fluid flow in the transversely isotropic fissured rocks, *Comput. Geotech.* 128 (2020) 103812, <http://dx.doi.org/10.1016/j.comgeo.2020.103812>.
- [29] Q. Zhang, X. Yan, J. Shao, Fluid flow through anisotropic and deformable double porosity media with ultra-low matrix permeability: A continuum framework, *J. Pet. Sci. Eng.* 200 (2021) 108349, <http://dx.doi.org/10.1016/j.petrol.2021.108349>.
- [30] N. Khalili, S. Valliappan, C.F. Wan, Consolidation of Fissured clays, *Géotechnique* 49 (1) (1999) 75–89, <http://dx.doi.org/10.1680/geot.1999.49.1.75>.

- [31] N. Khalili, M.H. Khabbaz, S. Valliappan, An effective stress based numerical model for hydro-mechanical analysis in unsaturated porous media, *Comput. Mech.* 26 (2) (2000) 174–184, <http://dx.doi.org/10.1007/s004660000165>.
- [32] N. Khalili, R. Witt, L. Laloui, L. Vulliet, A. Koliji, Effective stress in double porous media with two immiscible fluids, *Geophys. Res. Lett.* 32 (15) (2005) L15309, <http://dx.doi.org/10.1029/2005GL023766>.
- [33] Z.-Y. Wang, Y.-F. Jin, Z.-Y. Yin, Y.-Z. Wang, A novel coupled NS-PFEM with stable nodal integration and polynomial pressure projection for geotechnical problems, *Int. J. Numer. Anal. Methods Geomech.* 46 (13) (2022) 2535–2560, <http://dx.doi.org/10.1002/nag.3417>.
- [34] J.T. Camargo, J.A. White, R.I. Borja, A macroelement stabilization for mixed finite element/finite volume discretizations of multiphase poromechanics, *Comput. Geosci.* 25 (2) (2021) 775–792, <http://dx.doi.org/10.1007/s10596-020-09964-3>.
- [35] X. Yan, Z. Huang, J. Yao, Y. Li, D. Fan, H. Sun, K. Zhang, An efficient numerical hybrid model for multiphase flow in deformable fractured-shale reservoirs, *SPE J.* 23 (04) (2018) 1412–1437, <http://dx.doi.org/10.2118/191122-PA>.
- [36] X. Yan, H. Sun, Z. Huang, L. Liu, P. Wang, Q. Zhang, J. Yao, Hierarchical modeling of hydromechanical coupling in fractured shale gas reservoirs with multiple porosity scales, *Energy & Fuels* 35 (7) (2021) 5758–5776, <http://dx.doi.org/10.1021/acs.energyfuels.0c03757>.
- [37] J.A. White, R.I. Borja, Stabilized low-order finite elements for coupled solid-deformation/fluid-diffusion and their application to fault zone transients, *Comput. Methods Appl. Mech. Engrg.* 197 (49–50) (2008) 4353–4366, <http://dx.doi.org/10.1016/j.cma.2008.05.015>.
- [38] Z.-Y. Wang, Y.-F. Jin, Z.-Y. Yin, Y.-Z. Wang, Overcoming volumetric locking in SNS-PFEM with cubic bubble function and selective integration, *Internat. J. Numer. Methods Engrg.* (2022) <http://dx.doi.org/10.1002/nme.7107>.
- [39] F. Brezzi, K.-J. Bathe, A discourse on the stability conditions for mixed finite element formulations, *Comput. Methods Appl. Mech. Engrg.* 82 (1–3) (1990) 27–57, [http://dx.doi.org/10.1016/0045-7825\(90\)90157-H](http://dx.doi.org/10.1016/0045-7825(90)90157-H).
- [40] M. Preisig, J.H. Prévost, Stabilization procedures in coupled poromechanics problems: A critical assessment, *Int. J. Numer. Anal. Methods Geomech.* 35 (11) (2011) 1207–1225, <http://dx.doi.org/10.1002/nag.951>.
- [41] C.R. Dohrmann, P.B. Bochev, A stabilized finite element method for the Stokes problem based on polynomial pressure projections, *Internat. J. Numer. Methods Fluids* 46 (2) (2004) 183–201, <http://dx.doi.org/10.1002/fld.752>.
- [42] E. Oñate, A stabilized finite element method for incompressible viscous flows using a finite increment calculus formulation, *Comput. Methods Appl. Mech. Engrg.* 182 (3–4) (2000) 355–370, [http://dx.doi.org/10.1016/S0045-7825\(99\)00198-X](http://dx.doi.org/10.1016/S0045-7825(99)00198-X).
- [43] G.-R. Liu, T.T. Nguyen, *Smoothed Finite Element Methods*, Taylor & Francis, Boca Raton, 2010.
- [44] G.-R. Liu, K.Y. Dai, T.T. Nguyen, A smoothed finite element method for mechanics problems, *Comput. Mech.* 39 (6) (2007) 859–877, <http://dx.doi.org/10.1007/s00466-006-0075-4>.
- [45] G.-R. Liu, The smoothed finite element method (S-FEM): A framework for the design of numerical models for desired solutions, *Front. Struct. Civ. Eng.* 13 (2) (2019) 456–477, <http://dx.doi.org/10.1007/s11709-019-0519-5>.
- [46] W. Zeng, G.-R. Liu, Smoothed finite element methods (S-FEM): An overview and recent developments, *Arch. Comput. Methods Eng.* 25 (2) (2018) 397–435, <http://dx.doi.org/10.1007/s11831-016-9202-3>.
- [47] C. Jiang, X. Han, G.-R. Liu, Z.-Q. Zhang, G. Yang, G.-J. Gao, Smoothed finite element methods (S-FEMs) with polynomial pressure projection (P3) for incompressible solids, *Eng. Anal. Bound. Elem.* 84 (2017) 253–269, <http://dx.doi.org/10.1016/j.enganabound.2017.07.022>.
- [48] H. Feng, X.Y. Cui, G.Y. Li, A stable nodal integration method with strain gradient for static and dynamic analysis of solid mechanics, *Eng. Anal. Bound. Elem.* 62 (2016) 78–92, <http://dx.doi.org/10.1016/j.enganabound.2015.10.001>.
- [49] M.A. Puso, J.-S. Chen, E. Zywicz, W. Elmer, Meshfree and finite element nodal integration methods, *Internat. J. Numer. Methods Engrg.* 74 (3) (2008) 416–446, <http://dx.doi.org/10.1002/nme.2181>.
- [50] Y.-F. Jin, Z.-Y. Yin, W.-H. Yuan, Simulating retrogressive slope failure using two different smoothed particle finite element methods: A comparative study, *Eng. Geol.* 279 (2020) 105870, <http://dx.doi.org/10.1016/j.enggeo.2020.105870>.
- [51] W. Zhang, W. Yuan, B. Dai, Smoothed particle finite-element method for large-deformation problems in geomechanics, *Int. J. Geomech.* 18 (4) (2018) 04018010, [http://dx.doi.org/10.1061/\(ASCE\)GM.1943-5622.0001079](http://dx.doi.org/10.1061/(ASCE)GM.1943-5622.0001079).
- [52] W.-H. Yuan, B. Wang, W. Zhang, Q. Jiang, X.-T. Feng, Development of an explicit smoothed particle finite element method for geotechnical applications, *Comput. Geotech.* 106 (2019) 42–51, <http://dx.doi.org/10.1016/j.compgeo.2018.10.010>.
- [53] Y.-F. Jin, Z.-Y. Yin, J. Li, J.-G. Dai, A novel implicit coupled hydro-mechanical SPFEM approach for modelling of delayed failure of cut slope in soft sensitive clay, *Comput. Geotech.* 140 (2021) 104474, <http://dx.doi.org/10.1016/j.compgeo.2021.104474>.
- [54] A. Shafee, A. Khoshghalb, An improved node-based smoothed point interpolation method for coupled hydro-mechanical problems in geomechanics, *Comput. Geotech.* 139 (2021) 104415, <http://dx.doi.org/10.1016/j.compgeo.2021.104415>.
- [55] A. Khoshghalb, A. Shafee, A. Toootoonchi, O. Ghaffariour, S.A. Jazaeri, Application of the smoothed point interpolation methods in computational geomechanics: A comparative study, *Comput. Geotech.* 126 (2020) 103714, <http://dx.doi.org/10.1016/j.compgeo.2020.103714>.
- [56] A.H.D. Cheng, Material coefficients of anisotropic poroelasticity, *Int. J. Rock Mech. Min. Sci.* 34 (2) (1997) 199–205, [http://dx.doi.org/10.1016/S0148-9062\(96\)00055-1](http://dx.doi.org/10.1016/S0148-9062(96)00055-1).
- [57] H.F. Wang, *Theory of Linear Poroelasticity with Applications To Geomechanics and Hydrogeology*, in: Princeton series in geophysics, Princeton University Press, Princeton, NJ, 2000.
- [58] A. Mehrabian, Y.N. Abousleiman, Theory and analytical solution to Cryer's problem of N-porosity and N-permeability poroelasticity, *J. Mech. Phys. Solids* 118 (2018) 218–227, <http://dx.doi.org/10.1016/j.jmps.2018.05.011>.
- [59] J. Choo, R.I. Borja, Stabilized mixed finite elements for deformable porous media with double porosity, *Comput. Methods Appl. Mech. Engrg.* 293 (2015) 131–154, <http://dx.doi.org/10.1016/j.cma.2015.03.023>.
- [60] R.I. Borja, Plasticity, Springer Berlin Heidelberg, Berlin, Heidelberg, 2013, <http://dx.doi.org/10.1007/978-3-642-38547-6>.
- [61] O. Coussy, Poromechanics, John Wiley & Sons, Ltd, Chichester, UK, 2003, <http://dx.doi.org/10.1002/0470092718>.

- [62] A.H.D. Cheng, Intrinsic material constants of poroelasticity, *Int. J. Rock Mech. Min. Sci.* 142 (2021) 104754, <http://dx.doi.org/10.1016/j.ijrmms.2021.104754>.
- [63] C. Liu, A. Mehrabian, Y.N. Abousleiman, Poroelastic dual-porosity/dual-permeability after-closure pressure-curves analysis in hydraulic fracturing, *SPE J.* 22 (01) (2017) 198–218, <http://dx.doi.org/10.2118/181748-PA>.
- [64] M. Ashworth, F. Doster, Foundations and their practical implications for the constitutive coefficients of poromechanical dual-Continuum models, *Transp. Porous Media* 130 (3) (2019) 699–730, <http://dx.doi.org/10.1007/s11242-019-01335-6>.
- [65] M. Ashworth, F. Doster, Anisotropic dual-continuum representations for multiscale poroelastic materials: Development and numerical modelling, *Int. J. Numer. Anal. Methods Geomech.* 44 (17) (2020) 2304–2328, <http://dx.doi.org/10.1002/nag.3140>.
- [66] S.C.Y. Ip, J. Choo, R.I. Borja, Impacts of saturation-dependent anisotropy on the shrinkage behavior of clay rocks, *Acta Geotech.* 16 (11) (2021) 3381–3400, <http://dx.doi.org/10.1007/s11440-021-01268-9>.
- [67] D. Elsworth, M. Bai, Flow-deformation response of dual-porosity media, *J. Geotech. Eng.* 118 (1) (1992) 107–124, [http://dx.doi.org/10.1061/\(ASCE\)0733-9410\(1992\)118:1\(107\)](http://dx.doi.org/10.1061/(ASCE)0733-9410(1992)118:1(107).).
- [68] M. Bai, F. Meng, D. Elsworth, Y.N. Abousleiman, J.-C. Roegiers, Numerical modeling of coupled flow and deformation in fractured rock specimens, *Int. J. Numer. Anal. Methods Geomech.* 23 (2) (1999) 141–160.
- [69] W.K.S. Pao, R.W. Lewis, Three-dimensional finite element simulation of three-phase flow in a deforming fissured reservoir, *Comput. Methods Appl. Mech. Engrg.* 191 (23–24) (2002) 2631–2659, [http://dx.doi.org/10.1016/S0045-7825\(01\)00420-0](http://dx.doi.org/10.1016/S0045-7825(01)00420-0).
- [70] X. Yan, Z. Huang, J. Yao, Z. Zhang, P. Liu, Y. Li, D. Fan, Numerical simulation of hydro-mechanical coupling in fractured vuggy porous media using the equivalent continuum model and embedded discrete fracture model, *Adv. Water Resour.* 126 (2019) 137–154, <http://dx.doi.org/10.1016/j.advwatres.2019.02.013>.
- [71] M. Bai, Q. Ma, J.-C. Roegiers, Dual-porosity behaviour of naturally fractured reservoirs, *Int. J. Numer. Anal. Methods Geomech.* 18 (6) (1994) 359–376, <http://dx.doi.org/10.1002/nag.1610180602>.
- [72] J.-S. Chen, C.-T. Wu, S. Yoon, Y. You, A stabilized conforming nodal integration for Galerkin mesh-free methods, *Internat. J. Numer. Methods Engrg.* 50 (2) (2001) 435–466.
- [73] S. Beissel, T. Belytschko, Nodal integration of the element-free Galerkin method, *Comput. Methods Appl. Mech. Engrg.* 139 (1–4) (1996) 49–74, [http://dx.doi.org/10.1016/S0045-7825\(96\)01079-1](http://dx.doi.org/10.1016/S0045-7825(96)01079-1).
- [74] N. Guo, Z. Yang, W. Yuan, J. Zhao, A coupled SPFEM/DEM approach for multiscale modeling of large-deformation geomechanical problems, *Int. J. Numer. Anal. Methods Geomech.* 45 (5) (2021) 648–667, <http://dx.doi.org/10.1002/nag.3175>.
- [75] M.A. Puso, J. Solberg, A stabilized nodally integrated tetrahedral, *Internat. J. Numer. Methods Engrg.* 67 (6) (2006) 841–867, <http://dx.doi.org/10.1002/nme.1651>.
- [76] H. Wei, J.-S. Chen, M. Hillman, A stabilized nodally integrated meshfree formulation for fully coupled hydro-mechanical analysis of fluid-saturated porous media, *Comput. & Fluids* 141 (2016) 105–115, <http://dx.doi.org/10.1016/j.compfluid.2015.11.002>.
- [77] H. Wei, J.-S. Chen, F. Beckwith, J. Baek, A naturally stabilized semi-Lagrangian meshfree formulation for multiphase porous media with application to landslide modeling, *J. Eng. Mech.* 146 (4) (2020) 04020012, [http://dx.doi.org/10.1061/\(ASCE\)EM.1943-7889.0001729](http://dx.doi.org/10.1061/(ASCE)EM.1943-7889.0001729).
- [78] W. Sun, J.T. Ostien, A.G. Salinger, A stabilized assumed deformation gradient finite element formulation for strongly coupled poromechanical simulations at finite strain, *Int. J. Numer. Anal. Methods Geomech.* 37 (16) (2013) 2755–2788, <http://dx.doi.org/10.1002/nag.2161>.
- [79] X. Yan, Z. Huang, J. Yao, Y. Li, D. Fan, An efficient embedded discrete fracture model based on mimetic finite difference method, *J. Pet. Sci. Eng.* 145 (2016) 11–21, <http://dx.doi.org/10.1016/j.petrol.2016.03.013>.
- [80] Y.N. Abousleiman, A.H.D. Cheng, L. Cui, E. Detournay, J.-C. Roegiers, Mandel's problem revisited, *Géotechnique* 46 (2) (1996) 187–195, <http://dx.doi.org/10.1680/geot.1996.46.2.187>.
- [81] T. Aoki, C.P. Tan, W.E. Bamford, Effects of deformation and strength anisotropy on borehole failures in saturated shales, *Int. J. Rock Mech. Min. Sci. Geomech. Abstracts* 30 (7) (1993) 1031–1034, [http://dx.doi.org/10.1016/0148-9062\(93\)90067-N](http://dx.doi.org/10.1016/0148-9062(93)90067-N).
- [82] S. Valliappan, N. Khalili, Flow through fissured porous media with deformable matrix, *Internat. J. Numer. Methods Engrg.* 29 (5) (1990) 1079–1094, <http://dx.doi.org/10.1002/nme.1620290512>.
- [83] K. Pruess, T.N. Narasimhan, A practical method for modeling fluid and heat flow in fractured porous media, *Soc. Petrol. Eng. J.* 25 (01) (1985) 14–26, <http://dx.doi.org/10.2118/10509-PA>.
- [84] Q. Zhang, X. Yan, Z. Li, A mathematical framework for multiphase poromechanics in multiple porosity media, *Comput. Geotech.* 146 (2022) 104728, <http://dx.doi.org/10.1016/j.compgeo.2022.104728>.
- [85] R.N. Horne, *Modern Well Test Analysis: A Computer-Aided Approach*, second ed., Petroway, Palo Alto, CA, 1995.
- [86] A.H.D. Cheng, P. Sidauruk, Y.N. Abousleiman, Approximate inversion of the Laplace transform, *Math. J.* 4 (2) (1994) 76–82.
- [87] Y. Zhao, S.J. Semnani, Q. Yin, R.I. Borja, On the strength of transversely isotropic rocks, *Int. J. Numer. Anal. Methods Geomech.* 42 (16) (2018) 1917–1934, <http://dx.doi.org/10.1002/nag.2809>.
- [88] S.J. Semnani, J.A. White, R.I. Borja, Thermoplasticity and strain localization in transversely isotropic materials based on anisotropic critical state plasticity, *Int. J. Numer. Anal. Methods Geomech.* 40 (18) (2016) 2423–2449, <http://dx.doi.org/10.1002/nag.2536>.
- [89] H. Niandou, J.F. Shao, J.P. Henry, D. Fourmaintraux, Laboratory investigation of the mechanical behaviour of Tournemire shale, *Int. J. Rock Mech. Min. Sci.* 34 (1) (1997) 3–16, [http://dx.doi.org/10.1016/S1365-1609\(97\)80029-9](http://dx.doi.org/10.1016/S1365-1609(97)80029-9).
- [90] S.C.Y. Ip, R.I. Borja, Evolution of anisotropy with saturation and its implications for the elastoplastic responses of clay rocks, *Int. J. Numer. Anal. Methods Geomech.* 46 (1) (2022) 23–46, <http://dx.doi.org/10.1002/nag.3289>.
- [91] F. Valès, D. Nguyen Minh, H. Gharbi, A. Rejeb, Experimental study of the influence of the degree of saturation on physical and mechanical properties in Tournemire shale (France), *Appl. Clay Sci.* 26 (1–4) (2004) 197–207, <http://dx.doi.org/10.1016/j.clay.2003.12.032>.
- [92] Y. Zhao, R.I. Borja, A double-yield-surface plasticity theory for transversely isotropic rocks, *Acta Geotech.* (2022) <http://dx.doi.org/10.1007/s11440-022-01605-6>.

- [93] C. Callari, F. Armero, Finite element methods for the analysis of strong discontinuities in coupled poro-plastic media, *Comput. Methods Appl. Mech. Engrg.* 191 (39–40) (2002) 4371–4400, [http://dx.doi.org/10.1016/S0045-7825\(02\)00374-2](http://dx.doi.org/10.1016/S0045-7825(02)00374-2).
- [94] Z. Wang, Q. Zhang, W. Zhang, A novel collaborative study of abnormal roof water inrush in coal seam mining based on strata separation and wing crack initiation, *Eng. Fail. Anal.* 142 (2022) 106762, <http://dx.doi.org/10.1016/j.engfailanal.2022.106762>.
- [95] Q. Zeng, J. Yao, J.F. Shao, Study of hydraulic fracturing in an anisotropic poroelastic medium via a hybrid EDFM-XFEM approach, *Comput. Geotech.* 105 (2019) 51–68, <http://dx.doi.org/10.1016/j.compgeo.2018.09.010>.
- [96] A. Mehrabian, Y.N. Abousleiman, Gassmann equations and the constitutive relations for multiple-porosity and multiple-permeability poroelasticity with applications to oil and gas shale, *Int. J. Numer. Anal. Methods Geomech.* 39 (14) (2015) 1547–1569, <http://dx.doi.org/10.1002/nag.2399>.
- [97] R.W. Lewis, B.A. Schrefler, *The Finite Element Method in the Static and Dynamic Deformation and Consolidation of Porous Media*, second ed., John Wiley, Chichester, 1998.
- [98] P. Sarma, K. Aziz, New transfer functions for simulation of naturally fractured reservoirs with dual porosity models, *SPE J.* 11 (03) (2006) 328–340, <http://dx.doi.org/10.2118/90231-PA>.
- [99] T. Ahmed, Fractured reservoirs, in: *Reservoir Engineering Handbook*, Elsevier, 2010, pp. 1338–1432, <http://dx.doi.org/10.1016/B978-1-85617-803-7.50025-0>.